Overlapping turbulent boundary layers in an energetic coastal sea

Arnaud F. Valcarcel[1,2,3], Craig L. Stevens[2,4], Joanne M. O'Callaghan[3,4], and Sutara H. Suanda[5]

[1]University of Otago, Department of Marine Science, Dunedin, New Zealand
[2]National Institute of Water and Atmospheric research, Ocean Observations, Wellington, New Zealand
[3]Oceanly Science Limited, Wellington, New Zealand
[4]University of Auckland, Department of Physics, Auckland, New Zealand
[5]University of North Carolina in Wilmington, Department of Physics and Physical Oceanography, Wilmington, USA

Correspondence: Arnaud F. Valcarcel (arnaud@oceanlyscience.com)

Abstract. Turbulent mixing properties were directly observed to understand the interactions and overlapping events of wind- and tidally-forced boundary layers in a deep, weakly-stratified coastal sea. Te-Moana-o-Raukawa/Cook Strait of Aotearoa New Zealand is an $\mathcal{O}(200\,\mathrm{m})$-deep, energetic strait, known to experience both strong tidal currents and high wind speeds. More than $\mathcal{O}(40,000)$ quality-controlled turbulence observations were obtained from an ocean glider equipped with a microstructure profiler and a current speed through water sensor. Tidal flows of $\mathcal{O}(1\,\mathrm{m\,s^{-1}})$ and wind speeds of $\mathcal{O}(10\,\mathrm{m\,s^{-1}})$ independently enhanced turbulent dissipation to $\epsilon = \mathcal{O}(10^{-5}\,\mathrm{W\,kg^{-1}})$ in bottom and surface mixed layers. Over a four-day period, boundary-generated turbulence was evident in the interior water column on ten occasions, enhancing interior diapycnal diffusivity levels by 5-35-fold, reaching $K_z = \mathcal{O}(0.1 - 1\,\mathrm{m^2\,s^{-1}})$.On three instances, the surface and bottom mixed layers overlapped. These overlapping boundary layers were present in water depths five-times deeper than previously observed, which has implications for the vertical extent of material fluxes from the surface or seafloor. Interior stratification was transient, emerging from far-field advection of low density surface waters and supported by vertical buoyancy fluxes, that were episodically eroded by boundary-generated turbulence. Combining observations with one-dimensional General Ocean Turbulence Model (GOTM) outputs, turbulence interactions in the interior were found to be modulated by wind, tides and transient stratification fields, in turn influencing the vertical structure of sinks and sources of turbulent kinetic energy. Enhanced vertical transport toward the interior of the near-boundary shear-produced turbulence was found to erode interior stratification. The interplay between antecedent stratification, turbulence generation, and vertical transport allowed boundary layers to interact and modulate the vertical structure of seawater properties in deep coastal passages.

1 Introduction

Turbulent mixing regulates stratification, air-sea exchanges and nutrient fluxes in the coastal ocean (Sharples et al., 2001; MacKinnon and Gregg, 2005; Bianchi et al., 2005). Variability in vertical and horizontal mixing patterns and mechanics has regional and global implications for biological productivity and the uptake of atmospheric carbon dioxide (Thomas et al., 2004; Borges et al., 2005; Simpson and Sharples, 2012; Becherer et al., 2022). Ocean turbulence is primarily focused in the surface and bottom boundary layers, where wind stress and tidal currents, respectively, generate turbulent kinetic energy

(TKE) through shear-driven instabilities and wave breaking, leading to mixing (Waterhouse et al., 2014; Wang et al., 2014; Callaghan et al., 2014; Esters et al., 2018; Trowbridge and Lentz, 2018). Turbulence can be confined to each boundary layer independently, but can also extend into the water column, leading to an interaction between the two boundaries. Surface and bottom boundary layers can overlap in shallow $< \mathcal{O}(40\,\mathrm{m})$ coastal waters (Gargett and Wells, 2007; Nimmo Smith et al., 1999; Schultze et al., 2020) but it is uncommon in the deeper ocean (Yan et al., 2022). Vertical separation of the boundary layers and/or inhibition by stratification within the water column interior are typically sufficient to prevent overlaps. Studying the stratification configuration and vertical turbulent exchanges that allow turbulent boundary layers to interact in deep passages is essential to understand the extent to which mixing controls biophysical processes in all regions of the coastal ocean.

At the ocean surface, the boundary layer expands in relation to competing processes that either actively mix water properties (e.g., wind-driven shear instabilities, wave breaking) or increase stratification (e.g., solar heating, buoyancy fluxes). The balance of processes ultimately controls the transport of heat, gases, and mass across the air-sea boundary and into the ocean interior (Sutherland et al., 2014; Esters et al., 2018; Giunta and Ward, 2022). Near the seafloor, the bottom boundary layer originates by the complex interactions between oscillatory tidal currents, stratification and seabed topography (Gayen et al., 2010). Each layer is characterised by elevated TKE dissipation rates ($\epsilon\,[\mathrm{W\,kg^{-1}}]$) and weak background stratification ($N\,[\mathrm{s^{-1}}]$), termed the surface (SML) and bottom (BML) mixed layer, respectively. In the SML and BML, quasi-homogeneous tracer concentrations illustrate the outcome of past mixing (Esters et al., 2018; Giunta and Ward, 2022). Representing actively-mixing turbulence, ϵ is highest near the boundary where TKE production is dominated by shear-driven processes, and usually decreases with distance to the boundary in each layer (MacKinnon and Gregg, 2005; Sutherland et al., 2014; Milne et al., 2017).

Based on the assumption that irreversible mixing rates and turbulent fluxes are dominated by large-scale turbulent kinetic energy production and eddy motions (Bouffard and Boegman, 2013; Osborn, 1980), diapycnal diffusivity ($K_z\,[\mathrm{m^2\,s^{-1}}]$), the measure of turbulence-driven diffusive fluxes across isopycnals, can be estimated from measurements of ϵ and N as:

$$K_z \leq \Gamma\frac{\epsilon}{N^2} \tag{1}$$

with Γ the efficiency coefficient for irreversible mixing, generally taken as 0.2, its canonical value, when direct estimates are not available (Gregg et al., 2018). Nevertheless, variation in Γ has been observed in numerical simulations, and field and laboratory measurements. The cause of variability, in particular near surface and bottom boundaries remains unresolved (see Monismith et al. (2018) for a comprehensive review). Fully-developed isotropic turbulence is expected for $K_z > 100 \times \nu\Gamma \sim 3 \times 10^{-5}\,\mathrm{m^2\,s^{-1}}$ (i.e. a buoyancy Reynolds number $Re_b > 100$), with $\nu\,[\mathrm{m^2\,s^{-1}}]$ the kinematic viscosity (Schultze et al., 2017; Bouffard and Boegman, 2013; Shih et al., 2005). In the ocean interior, overlapping of boundary layers likely elevate ϵ and K_z from otherwise quiescent levels (Schultze et al., 2020; Yan et al., 2022). In similar proportions as when, e.g., internal waves break (e.g. interactions between boundary-produced turbulence and interior stratification) or turbulence bursts are ejected from the boundary layers (Thorpe et al., 2008; Gayen et al., 2010; Zhang and Tian, 2014; Wang et al., 2014).

Using Large Eddy Simulation (LES) of a $45\,\mathrm{m}$-deep water column, Yan et al. (2022) concluded that in "intermediate-depth" ocean systems where surface and bottom boundary layers coexist, boundary layer overlapping can occur when interior

stratification is weak and water depths are shallow. We employ a well-tested turbulence model (GOTM, Burchard et al. (1999); Umlauf and Burchard (2005)) to isolate features of overlapping boundary layers in a deep, energetic system.

Directly observing turbulent dynamics of ocean boundary layers remains a challenge (Jabbari and Boegman, 2021). In recent years, ocean gliders have proven to be a robust platform to expand understanding of ocean turbulence, largely due to the increased quantities of data. Gliders are autonomous underwater vehicles (AUVs) that use a buoyancy engine for locomotion and power-efficient remote sampling (Jones et al., 2005; Rudnick, 2016). The buoyancy propulsion engine means that gliders are relatively quiet platforms, well-suited to turbulence sampling in a range of weather conditions, including strong winds (Fer et al., 2014; Peterson and Fer, 2014; Schultze et al., 2020). Sensors mounted on gliders allow for direct measurements of mean flow properties and turbulence-driven mixing dynamics.

Here, we present direct ocean glider observations and model evaluation of the dynamics of overlapping wind- and tidally-forced boundary layers in an energetic coastal sea. The overarching objective of this work is to understand turbulent mixing dynamics when wind and tide-driven boundary turbulence interact in the interior and the mixed layers overlap. Specifically, (1) What are the *in situ* turbulence characteristics of mixed layer overlapping? (2) What is the sensitivity of these characteristics to observing methods? (3) What is the vertical partition of turbulence sources and sinks when mixed layers overlap? (4) And finally, what are the implications of enhanced overlapping-driven mixing for coastal ocean processes? The datasets and methodology are introduced in Section 2, and the observations and model results are presented in Section 3. In Section 4, the *in situ* observations and 1-D model outputs are discussed. Concluding remarks are provided in Section 5.

2   Methods

Overlapping boundary layers were examined using the following field and modelling approaches: 1) turbulence from an ocean microstructure glider (OMG), 2) flow conditions from a moored acoustic Doppler current profiler (ADCP), 3) wind forcing from an automatic weather station, and 4) turbulence balance terms calculated using the General Ocean Turbulence Model (GOTM), set up using observations from Te-Moana-o-Raukawa/Cook Strait.

The study site is a deep and wide, topographically complex passage that separates the two main islands of Aotearoa New Zealand, Te-Moana-o-Raukawa/Cook Strait (Fig. 1). The central constriction, the Narrows Basin, is on average $210\,\mathrm{m}$ deep, $22\,\mathrm{km}$ wide, and $20\,\mathrm{km}$ long. It is a natural laboratory to study overlapping boundary layers as it experiences both fast tidally driven flows, with maximum $U \sim 3.4\,\mathrm{m\,s^{-1}}$ during spring tides, and routinely has strong winds, exceeding $20\,\mathrm{m\,s^{-1}}$ (Vennell and Collins, 1991; Stevens et al., 2012; Turner et al., 2019).

Tidal currents in the Te-Moana-o-Raukawa/Cook Strait field region are primarily hydraulically-driven by a $140°$ phase difference of the M_2 constituent across Greater Te-Moana-o-Raukawa/Cook Strait (Heath, 1986; Vennell and Collins, 1991; Vennell, 1998a, b). In addition, strong winds funnel through the strait predominantly along the North-South axis due to the narrow oceanic gap between mountain ranges on the North and South Islands (Vennell and Collins, 1991; Zeldis et al., 2013; Stevens, 2014). Stevens (2018) sampled turbulent mixing in the region over three days using a loose-tethered Vertical Microstructure Profiler (VMP) and showed high levels of dissipation rates (linear average of $\epsilon = 2 \times 10^{-6}\,\mathrm{W\,kg^{-1}}$) in a low stratification
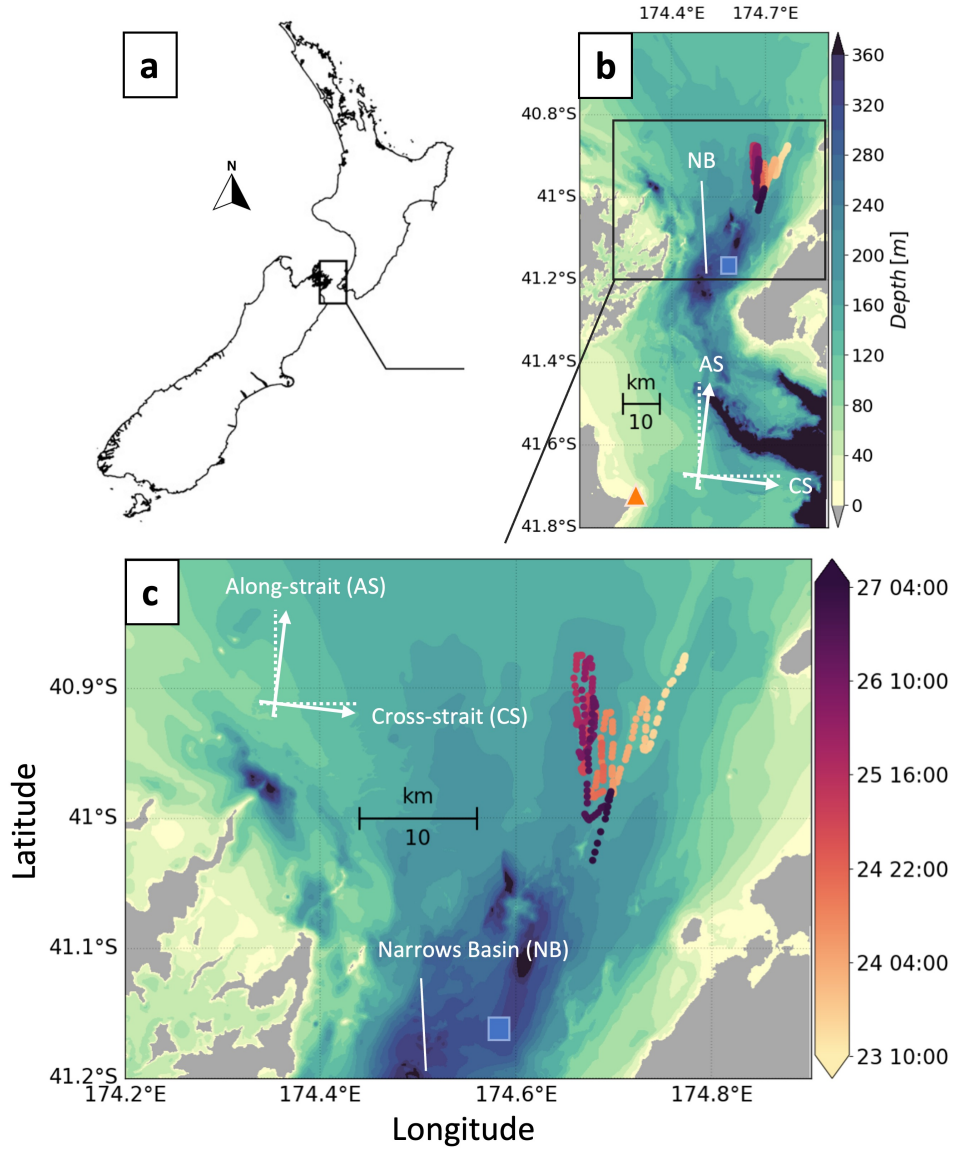
Figure 1. Maps of (a) Aotearoa New Zealand; Location of (b) the ADCP (blue square marker), the Cape Campbell atmospheric sampling station (orange triangle marker), the glider surfacing locations (colored circular markers) and the topography of Te-Moana-o-Raukawa/Cook Strait (colorbar); (c) a zoomed-in window showing the current profiler and the glider surfacing tracks coloured per time of the sampling window. In both panels, the Narrows Basin and the along/cross-strait directions are indicated in white.

$(10^{-7} < N^2 < 10^{-4}\,\mathrm{s}^{-1})$ environment. Environmental conditions of $< 10\,\mathrm{m\,s}^{-1}$ winds and $< 1.5\,\mathrm{m\,s}^{-1}$ mid water-column currents caused elevated diapycnal diffusivity (K_z) peaking close to $1\,\mathrm{m}^2\,\mathrm{s}^{-1}$. Nevertheless, weak vertical stratification was

found to persist in the strait (Stevens, 2014, 2018; Jhugroo et al., 2020) and boundary-driven mixing was not explicitly observed (Stevens, 2018).

2.1 In situ observations

Ocean glider and ADCP mooring observations (O'Callaghan and Elliott (2022), Valcarcel et al. (2022)) were obtained during June 2020 for Project CookieMonster (Cook strait Internal Energetics MONintoring and SynThEsis Research) using RV Kaharoa. The OMG completed a 20-day mission spanning 23 June -13 July. The moored ADCP was deployed at $174.5813°E$, $41.1651°S$ for six days spanning 22-27 June. Herein, we focus on the 23-27 June 2020 period of concurrent OMG and ADCP sampling, when wind and tidally generated boundary layers overlapped.

2.1.1 Glider-based turbulent microstructure

A Teledyne Webb Research Slocum glider was equipped with a MicroRider-1000EM turbulence profiler (Rockland Scientific Instruments) and a CTD (SeaBird Electronics), mounted on the top and side of the glider body, respectively. A relatively novel electromagnetic (EM) sensor was attached close to the shear probes on the nose of the MicroRider which directly measured flow past the sensors, providing an independent estimate of vehicle speed. A total of 257 co-located profiles of microstructure shear and temperature are presented here. Both up and downcasts of microstructure were obtained, however CTD profiles were only collected downward to conserve vehicle power. Each upward salinity profile (n) is estimated from the upward microstructure temperature profile (n) and the T-S relationship from the preceding downward profile (n-1).

High frequency ($512\,\text{Hz}$) measurements of the $\sim 5\,\text{mm}$-scale orthogonal ($\partial w/\partial x$, $\partial v/\partial x$) components of velocity shear in the reference frame of the glider, where the x coordinate is the glider path, were obtained using the two orthogonally-mounted airfoil shear probes of the MicroRider (O'Callaghan and Elliott, 2022). Estimates of turbulent kinetic energy dissipation rates ϵ and kinematic viscosity ν were computed using the Matlab codes developed by Rockland Scientific Instruments, the MicroRider manufacturer (RSI Odas library version 4.3.08, Lueck (2016)). Initially, isotropy of turbulence is assumed and implies that, for each probe, the dissipation rate of turbulent kinetic energy ϵ can be estimated from the shear spectra following Oakey (1982):

$$\epsilon = \frac{15}{2}\nu \overline{\left(\frac{\partial u_i}{\partial x}\right)^2} = \frac{15}{2}\nu \int_0^\infty \Phi(k)dk \quad [\text{W}\,\text{kg}^{-1}], \tag{2}$$

where $u_i = \{v; w\}$ are the velocity components orthogonal to the path of the glider, Φ is the shear spectra in wave number (k) space. Integration of shear spectra are computed in segments of $8\,\text{s}$ with $4\,\text{s}$ overlap and a $2\,\text{s}$ Fast Fourier Transform segment length, yielding $54,300$ ϵ estimates, with on average an estimate every $0.61\,\text{m}$.

Quantifying glider-based microstructure is a challenge as the vehicle axial speed through the water, U, is generally computed using a glider flight model based on the pressure gradient and angle of attack of the vehicle (Merckelbach et al., 2010, 2019).

Using in situ electromagnetic current meter data has been shown to improve by 10% the accuracy of shear-based ϵ estimates, where most U differences were attributed to flow variability (Merckelbach et al., 2019). To maximise confidence in the turbu-

lence data for an energetic system like Te-Moana-o-Raukawa/Cook Strait, we collected direct electromagnetic current (EMC) measurements of speed past the sensors to quantify U. The EMC sensor (AEM1-G, JFE Advantech Co., Ltd) measured flow speed by electromagnetic induction (Hall effect) at $0.5\,\mathrm{cm\,s^{-1}}$ accuracy, assuming a $1\,\mathrm{cm\,s^{-1}}$ reading uncertainty (Rockland Scientific, 2017; Merckelbach et al., 2019). The EMC measurements permitted raw counts to be converted into physical units of shear, and frequency into wave number (k) for spectral analysis. The glider speed sensor estimates ranged in $0.05-0.55\,\mathrm{m\,s^{-1}}$, averaging ($\pm 1$ standard deviation) to $0.34\,(\pm 0.04)\,\mathrm{m\,s^{-1}}$.

Unreliable ϵ estimates were removed from the analysis using the following criteria:

1. A minimum threshold for glider speeds of $U = 0.20\,\mathrm{m\,s^{-1}}$ filters out periods when the glider is not ascending/descending at a stable rate, removing sharp speed changes and inflection points. This removed 14.8% of total points.

2. If simultaneous ϵ estimates differ by an order of magnitude or more, the greater estimate is disregarded, otherwise the average value of estimates is used (Scheifele et al., 2018). This removed 1.5% of total points.

3. If glider speeds $U < 5(\epsilon/N)^{1/2}$, i.e. lower than 5 times the turbulent flow velocities, Taylor's frozen field hypothesis is likely invalid (Fer et al., 2014) and ϵ disregarded (Scheifele et al., 2018). This procedure removed 2.3% of total estimates.

A total of $43,300$ reliable ϵ estimates were used herein to examine overlapping boundary layers.

2.1.2 ADCP Mooring and ancillary observations

The seabed mooring comprised an upward-facing ADCP (Nortek instruments) and a SBE 37 Conductivity-Temperature-Depth sensor (CTD, SeaBird Electronics). ADCP current velocities were sampled at $1\,\mathrm{Hz}$, in $5\,\mathrm{m}$ bins between 35 to $295\,\mathrm{m}$ in water depth. Surface bins were discarded due to side-lobe interference. Velocities were filtered using an hourly first-order low-pass filter and decomposed into along- and cross-strait components (semi-major axis rotated $7°$ clockwise from true north, Figure 1). Vertical shear was computed using the along- and cross-strait velocity components.

Hourly meteorological measurements from the Cape Campbell Automatic Weather Station, $\sim 50\,\mathrm{km}$ away from the area of interest, were included in this analysis (Valcarcel et al., 2022). Along- and cross-strait components of wind speeds at 10m from the water surface were then estimated using a Hellman power law (Hellmann, 1919; Haas et al., 2021). Daily satellite averages of sea surface temperature (SST) with a $0.01°$ resolution (JPL MUR MEaSUREs Project, 2015) were also used, to provide context to subsurface temperature patterns in the glider observations.

2.2 Mixing analysis

Potential temperature θ and density σ were computed from *in situ* measurements of temperature and practical salinity using the Gibbs SeaWater TEOS-10 formulation (Ioc et al., 2010). Potential density profiles were re-ordered ($\sigma^\star$) to be monotonically increasing with depth, and used to compute the buoyancy frequency squared $N^2 = -g/\sigma_0^\star.\partial_z\sigma^\star\,[\mathrm{s^{-2}}]$ (Thorpe and Deacon, 1977; Mater et al., 2015), with g the gravitation constant and $\sigma_0^\star$ is the sorted potential density at a reference depth. For each profile, we identify the depths of the surface (SML) and bottom (BML) mixed layers, i.e. the top and bottom edges of the

stratified interior layer, using a potential temperature threshold of $\Delta\theta = 0.05\,°C$ under the assumption that it was a reliable proxy for homogeneity within a layer (Inall et al., 2021) as: $z_{top} = z(\theta > \theta_0 - \Delta\theta)$ [m] and $z_{bottom} = z(\theta < \theta_b + \Delta\theta)$ [m] where θ_0 and θ_b were the shallowest and deepest points in the profile respectively. This temperature change broadly represents the separation between near-boundary, weak-moderate stratification to interior elevated-strong N^2 (see Fig. 4 and Table 1). Overlapping mixed layers episodes are thus defined as periods when $z_{top} > z_{bottom}$.

We further describe periods of turbulence interactions in the interior, when ϵ is enhanced above a threshold value, whether the mixed layers overlap or not. We arbitrarily assume that boundary-generated turbulence interacts in the interior during periods when less than 10 successive data points in glider profiles ($\sim 6\,m$) are of weak dissipation, below $\epsilon_p = 3 \times 10^{-9}\,\mathrm{W\,kg^{-1}}$. The ϵ_p threshold is an order of magnitude below the mean, $3.3 \times 10^{-8}\,\mathrm{W\,kg^{-1}}$, and corresponds to the 15.8^{th} percentile of the ϵ distribution, i.e. a standard deviation below the median, $1.1 \times 10^{-8}\,\mathrm{W\,kg^{-1}}$. It was determined as a relevant value for identifying periods of interior turbulence interactions in both the observations and the GOTM data presented in this study, and is consistent with the commonly used dissipation thresholds to determine the extent of surface and bottom mixing layers (Sutherland et al., 2014; Esters et al., 2018; Giunta and Ward, 2022).

Diapycnal diffusivity is estimated through Eq. 1. Here Γ is set to 0.2, the canonical value for mixing efficiency. This choice is made as direct estimates of Γ are not available, and the community has not converged on a stable parameterization of Γ in all oceanic turbulence conditions (Gregg et al., 2018; Monismith et al., 2018; Mashayek et al., 2022). Variations of Γ with turbulence activity (i.e., Re_b) has however been extensively documented, and appears to represent well steady, homogeneous shear-driven turbulence (Shih et al., 2005; Bouffard and Boegman, 2013; Monismith et al., 2018). Therefore, in addition, to discuss the variations of diapycnal diffusivity in different Re_b conditions, we implement the Bouffard and Boegman (2013) parameterization of K_z (applied to OMG observations in e.g., Schultze et al. (2017)). Most ($\sim 99\%$) observations in the present study are of fully-developped isotropic turbulence, i.e. $Re_b > 100$. In this range, the Bouffard and Boegman (2013) parameterization is $\Gamma \equiv 2 \times Re_b^{-1/2}$ to estimate K_z with Eq. 1. The remaining samples are in the $7 < Re_b < 100$ "transitional regime" range, for which $\Gamma = 0.2$ is used in Eq. 1. For Re_b in $10^3 - 10^6$ (90% of points), parameterised Γ varies in $0.07 - 0.002$, differing from $\Gamma = 0.2$ by $68 - 99\%$. It should be noted that, within the mixed layers, near-boundary limitation of large overturning scales (i.e. large Re_b) may reduce Γ and K_z further, in unclear proportions (Bouffard and Boegman, 2013; Holleman et al., 2016; Monismith et al., 2018).

2.3 Physical separation of the sampling sites

The ADCP observations were used to provide a supplementary, semi-qualitative, tidal context to the OMG observations, and scale the magnitude of tidal forcing in the GOTM simulations. The glider was on average $27.6\,km$ from the ADCP (ranging in $19.7 - 35.9\,km$). Although separated by a relatively broad distance, we argue that shear and dissipation measurements can be qualitatively described within the same temporal framework, as the tidal excursion length characterizing the system is large. The tidal excursion length $L \equiv v_{peak}.T_{M2}/\pi$ ranged in $16.5 - 20.6\,km$ and quantifies the distance over which a fluid particle travels at peak flow speed ($|v| \in 1.2 - 1.5\,\mathrm{m\,s^{-1}}$) during one tidal cycle ($T_{M2} \sim 12\,h$), which was comparable to the average distance between sampling sites.

Depth-averaged currents sampled by the OMG were on average offset by 37 minutes from the moored ADCP measurements. This offset was more than double the phase-lag determined by Vennell (1998a), however the OMG data presented here was collected in a wider section of the strait where flows were less constricted and the tidal wave propagation is slower. Depth-averaged currents sampled by the OMG are also 73% of the amplitude of the ADCP measurements. This is most likely due to the flow constriction differences between the OMG and ADCP sites, the OMG site being significantly wider (Fig. 1). Using these considerations, background flow conditions for the OMG mission were inferred from the moored ADCP site, with a 37-minute lag and used to identify the periods of maximum and minimum shear. The 73% amplitude scaling was used to prescribe tidal forcing to GOTM (see the following section).

Along a transect between the ADCP site and the mean glider location, the bathymetry shallows and the channel width increases (Figure 1c). Along this distance, the phase of the cross-sectional averaged tidal velocity is approximately constant, characterizing Te-Moana-o-Raukawa/Cook Strait as a non-divergent short strait (Vennell, 1998a, b). During southward tidal flows, hydraulic acceleration could be expected to differentiate turbulence properties between sites. During northward flows, a submerged pinnacle, Fisherman's Rock, would be just outside the edge of the westernmost glider sampling position, and could affect turbulence structure by generating an eddy wake. For simplicity, and to focus the analysis on boundary layer processes, these effects were not considered in this analysis.

2.4 General Ocean Turbulence Model

GOTM is a one-dimensional model that computes solutions for the vertical Reynolds-Averaged Navier–Stokes equation for momentum, and temperature and salinity transport equations. A choice of closure schemes are available to calculate turbulent tracer flux (Umlauf and Burchard, 2005; Umlauf et al., 2012). Here, the two equation $(k-\epsilon)$ model solving for turbulent kinetic energy and a dissipative length scale (Canuto et al., 2001) was used. The turbulent kinetic energy (TKE, k) balance equation is represented by Reynolds decomposition in idealised Boussinesq-fluid formulation (Polzin and McDougall, 2022; Umlauf et al., 2012) as:

$$\dot{k} = T_k + P + G - \epsilon \quad [\text{W kg}^{-1}], \tag{3}$$

where $\dot{k}$ is the material derivative (includes temporal derivative and advection terms) of TKE. P, G and ϵ are the rates of shear production, buoyancy flux and dissipation of TKE, respectively. $T_k \equiv \partial_z(\nu \partial_z k)$, with ∂_z the vertical partial derivative. T_k, referenced hereafter as the "vertical transport" term, is the transport divergence and represents the contribution of all viscous and turbulent vertical transport terms (Yan et al., 2022; Becherer et al., 2022).

Behaviour of ϵ in a tidal- and wind-driven environment akin to Te-Moana-o-Raukawa/Cook Strait were examined. Model parameters were minimally tuned, similarly to the "Liverpool Bay" case used in the model development (Rippeth et al., 2001; Simpson et al., 2002; Verspecht et al., 2009). Salinity and temperature equations are solved with a 3h time-scale for relaxation to prescribed observations, interpolated to the GOTM timestep. This time-scale is representative of the mean duration of interior turbulence interactions and mixed layer overlapping events (3.4h, see Table 2), and a "Liverpool Bay" case input (Rippeth et al., 2001). Horizontal velocity components, pressure, salinity, temperature and TKE balance terms were computed
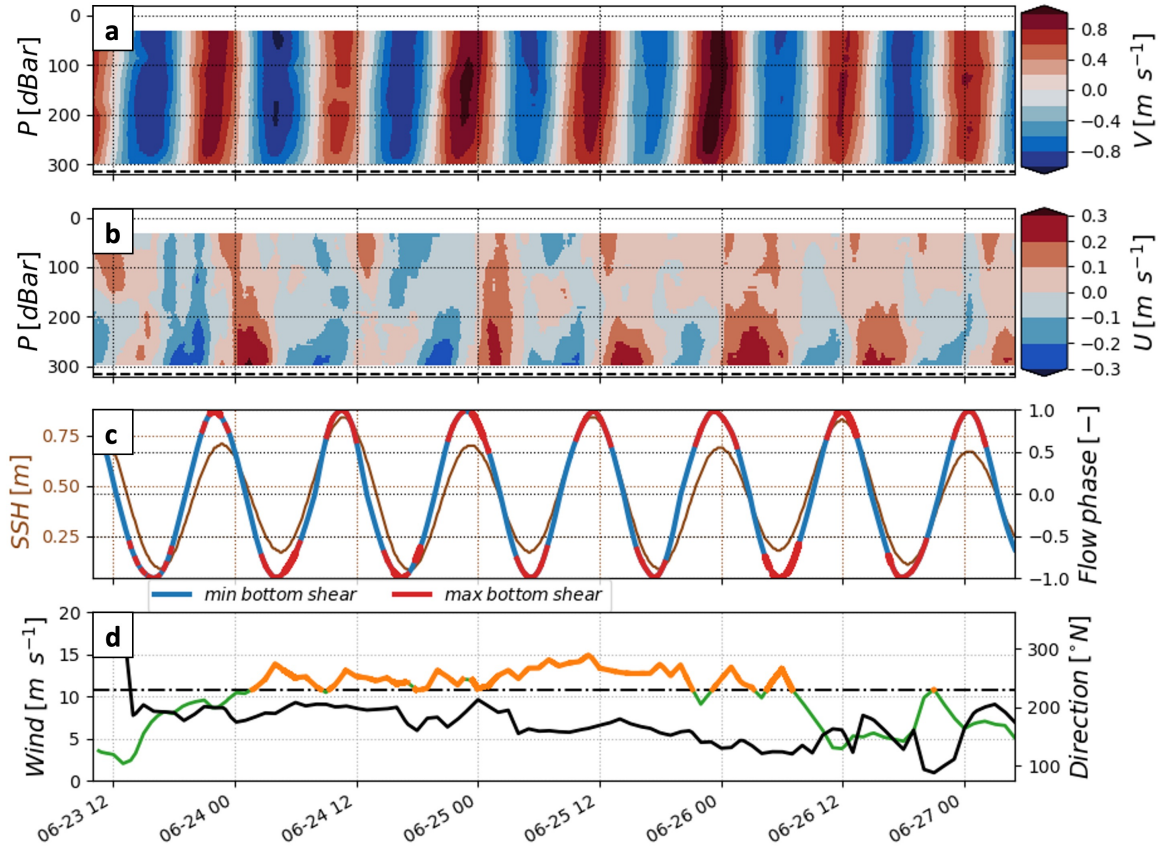
Figure 2. Large scale forcing of turbulent mixing at the study site, a combination of fast tidal flows and a strong wind perturbation. The figure shows depth-time series of (a) along and (b) cross-strait flow speeds (along the semi-major and semi-minor axes of the tidal ellipse respectively); time series of (c) sea surface height (brown axis and line) and along-strait tidal phase (red and blue mark maxima and minima in bottom shear respectively); time series of (d) wind speed below (green) and above (orange) the $10.8\,\mathrm{m\,s^{-1}}$ threshold described in the text (dashed line), and wind direction (from true North, black line), estimated at $10\,\mathrm{m}$ above sea-level from Cape Campbell weather station records. In panels a-b, the dashed line indicates the seafloor.

over 100 evenly-spaced levels of a $193\,\mathrm{m}$ depth (maximum water depth of the OMG data) with a $10\,\mathrm{s}$ integration time step. Scaled depth-averaged amplitudes of the dominant M2 tidal flows were used to force the external pressure gradient from tidal constituents. Air-sea interactions at the surface boundary were forced by horizontal momentum fluxes, using wind stress time series (Watanabe and Hibiya, 2002). Air-sea heat fluxes are assumed secondary. However, relaxation to observed T-S observations is assumed to account for heat flux processes e.g., night-time convection. Seabed interactions at the bottom boundary were prescribed with a typical bottom roughness length $h_{0b} = 0.004\,\mathrm{m}$ (i.e. hydrodynamical drag coefficient $C_d \sim$
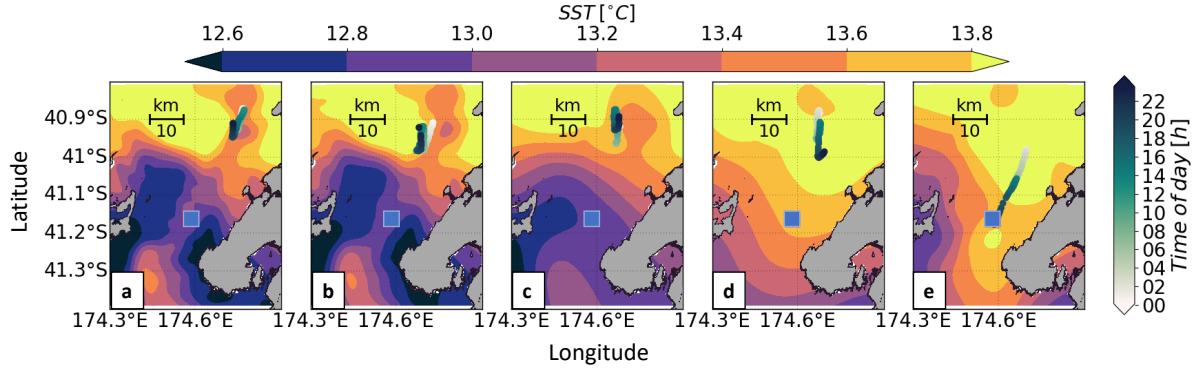
Figure 3. Overlay of OMG tracks and satellite-based SST measurements shows the connection between the observed "low density surface waters" and a larger scale surface temperature front. Maps of Te-Moana-o-Raukawa/Cook Strait with satellite SST fields (horizontal colorbar), ADCP site (blue square marker) and OMG surfacings per time of day (circular markers, vertical colorbar) for the days (a) 23rd, (b) 24th, (b) 25th, (b) 26th, (b) 27th of June.

2×10^{-3}). Background values of $10^{-10}\,\mathrm{m^2\,s^{-2}}$ and $10^{-12}\,\mathrm{W\,kg^{-1}}$ for k and ϵ were prescribed (Rippeth et al., 2001; Simpson et al., 2002; Verspecht et al., 2009).

3 Results

3.1 Background and forcing conditions

Flow speeds through Te-Moana-o-Raukawa/Cook Strait were dominated by the semi-diurnal spring tides, with along- and cross-strait speed components in the $\pm 1.5\,\mathrm{m\,s^{-1}}$ and $\pm 0.5\,\mathrm{m\,s^{-1}}$, respectively (Fig. 2 a,b). The larger, along-strait flows were oriented $7°$ from true North (not shown). Cross-strait tidal flows were $\sim 30\%$ slower but had greater vertical variability. The mean vertical structure of shear was similar for both directions of flow in the along-strait axis. Herein, we define the tidal phase of minimum and maximum bottom shear (mean $1.6 \times 10^{-5}\,\mathrm{s^{-2}}$ and $3.9 \times 10^{-6}\,\mathrm{s^{-2}}$ respectively, in the deepest $20\,\mathrm{m}$ of the dataset), to qualitatively contextualise near-bed turbulence structure with the temporality of the background tides (Fig. 2c).

Wind speeds ranged in $2 - 15\,\mathrm{m\,s^{-1}}$ over the period of the glider mission and mooring deployment (Fig. 2d). From 24 to 26 June, a two-day event of strong southwesterly winds funnelled through the strait with hourly wind speeds of $9 - 15\,\mathrm{m\,s^{-1}}$, peaking during the last four hours of 25 June. Low (green) and high (orange) wind periods were delineated using the $10.8\,\mathrm{m\,s^{-1}}$ threshold, to distinguish periods of calm to fresh breeze conditions, from strong breeze to near gale winds, on the empirical Beaufort scale. This scale and criteria are consistent with Schultze et al. (2020) methods, to facilitate comparison with turbulence generated under similar high wind-forcing conditions.

Daily-averaged SST fields show a warm surface layer from Greater Te-Moana-o-Raukawa/Cook Strait advected southwards through the Narrows over the same period (Fig. 3c). Several occurrences of notable high temperature, low density surface
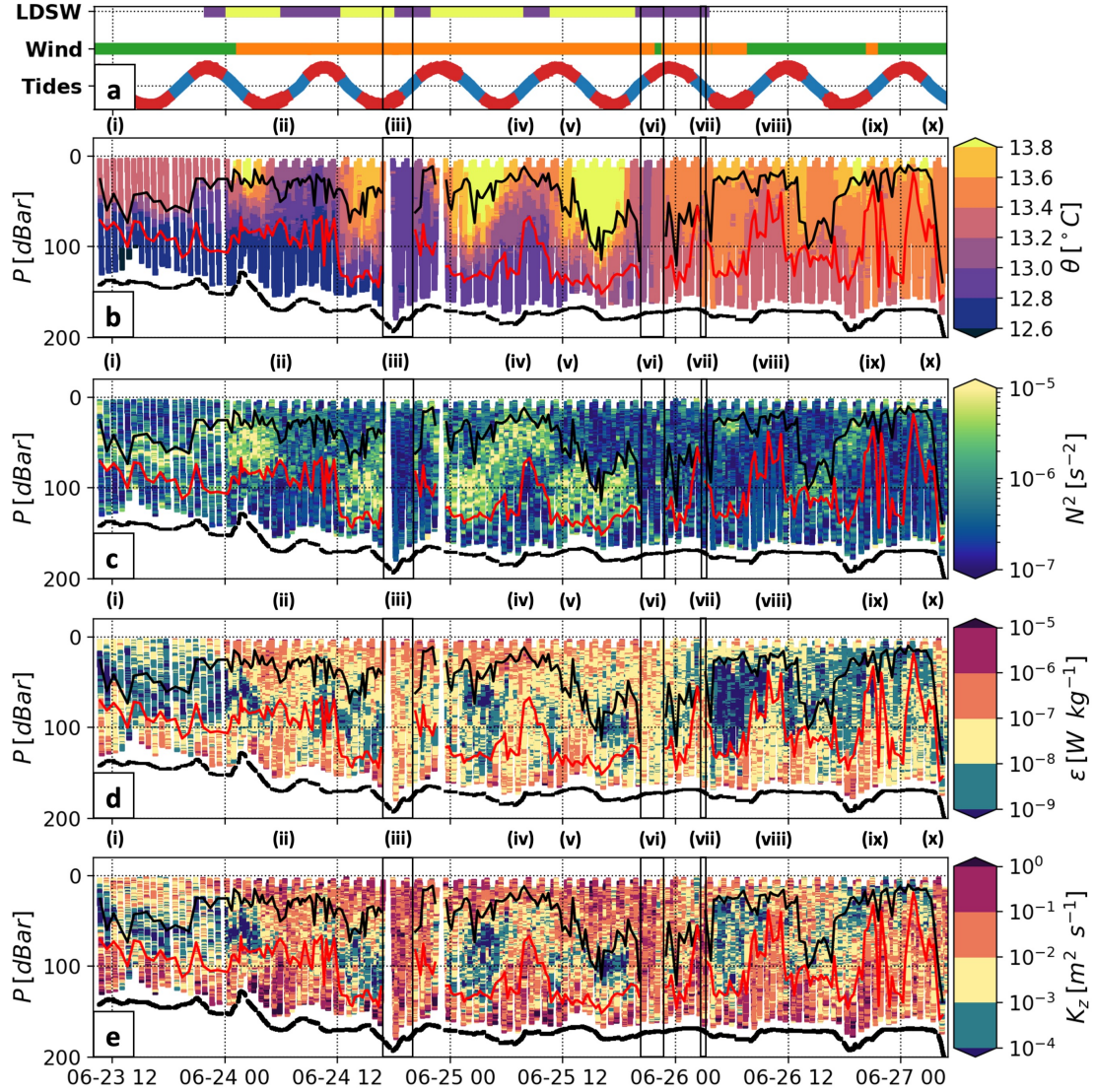
Figure 4. Variability of turbulence-driven mixing in a temperature-layered water column. Panel (a) shows the time windows for the low density surface waters (LDSW) episodes (purple and yellow top line), and bulk wind speed (green and orange middle line) and tidal shear (red and blue bottom sinusoid) variations. Panels (b-e) show the depth time series of Ocean Microstructure Glider observations of (b) potential temperature; (c) buoyancy frequency squared; (d) dissipation rates; (e) diapycnal diffusivity. For panels (b-e), the thick black dashed line is the seabed, and the surface (SML) and bottom mixed layer (BML) depths are shown with the black and red lines, respectively. For all panels, episodes of interior turbulence interactions are numbered (i-x) and the instances when mixed layers overlap episodes are marked with black solid rectangles.

Table 1. Reference table for the description of ranges of turbulent mixing variables in this study.

	Weak	Moderate	Elevated	Strong
$N^2\,[\mathrm{s^{-2}}]$	$< 10^{-7}$	$10^{-7} - 10^{-6}$	$10^{-6} - 10^{-5}$	$> 10^{-5}$
$\epsilon\,[\mathrm{W\,kg^{-1}}]$	$< 10^{-9}$	$10^{-9} - 10^{-7}$	$10^{-7} - 10^{-5}$	$> 10^{-5}$
$K_z\,[\mathrm{m^2\,s^{-1}}]$	$< 10^{-4}$	$10^{-4} - 10^{-2}$	$10^{-2} - 1$	> 1

waters (LDSW) were observed, likely related to the path of the glider crossing a surface front on several occasions (see also Fig. 4b). The verical extent of LDSW was from the surface down to $\sim 100\,\mathrm{m}$ when observed by the glider.

3.2 Boundary mixed layers and turbulence

Weakly-stratified conditions were observed throughout the sampling period, with potential temperatures ranging in $12.5 - 14\,^\circ\mathrm{C}$, vertical gradients smaller than $1\,^\circ\mathrm{C}$ and N^2 below $5 \times 10^{-5}\,\mathrm{s^{-2}}$ (Fig. 4a-c). The average thickness of the surface mixed layer (SML) was $43\,\mathrm{m}$, and ranged in $10 - 139\,\mathrm{m}$. The average thickness of the bottom mixed layer (BML) was $61\,\mathrm{m}$, and ranged from $22 - 150\,\mathrm{m}$. The averaged N^2 for the SML and BML was 10^{-6} and $6 \times 10^{-7}\,\mathrm{s^{-2}}$, respectively (Fig. 4c).

Interior stratification was distinct away from the SML and BML. Elevated N^2 values at the margins of the interior layer were 3×10^{-6} and $2 \times 10^{-6}\,\mathrm{s^{-2}}$, respectively (Fig. 4a-c). N^2 in the interior layer was up to three-fold greater than either the SML or BML with peaks co-located with strong temperature gradients. The interior layer had an average thickness of $63\,\mathrm{m}$ but was up to $125\,\mathrm{m}$ thick at times.

Enhanced dissipation rates were observed in the SML and BML of Te-Moana-o-Raukawa/Cook Strait (Fig. 4d). Intensified surface turbulence was focused in the upper $\sim 50\,\mathrm{m}$, and mostly confined to the SML. High dissipation in the SML was in the elevated range, episodically, in the top $10\,\mathrm{m}$. In the BML, there were elevated bottom-driven turbulence pulses with $10^{-7} < \epsilon < 10^{-4}\,\mathrm{W\,kg^{-1}}$ which ascended up to $75\,\mathrm{m}$ from the seabed at the semi-diurnal tidal frequency. Lower levels of dissipation were typically observed in the interior layer of the water column.

Elevated to strong levels of canonical diapycnal diffusivity, $K_z (\Gamma = 0.2)$, were primarily observed within the mixed layers (Fig. 4e). Fully-developed isotropic turbulence was observed for 98.9% of samples, with $K_z < 3 \times 10^{-5}\,\mathrm{m^2\,s^{-1}}$ only for 2.7% of interior layer samples, and 0.4% and none in the SML and BML, respectively. Diffusivity peaked to strong ($K_z > 1\,\mathrm{m^2\,s^{-1}}$) levels $< 20\,\mathrm{m}$ away from the seabed, where strong tidally-driven ϵ pulses acted against weak stratification (Fig. 4c-e). In the SML, K_z levels were in the elevated to strong range, during periods of intensified wind forcing, albeit with fewer strong samples than in the BML due to the relatively stronger stratification. When the mixed layers did not overlap, moderate to weak K_z was found in the interior, from the combination of moderate-weak dissipation and elevated-strong stratification.

The water column typically had intensified turbulence and diffusivity in both boundary layers and was highest in the BML (Fig. 5). The highest ϵ were found in the first 10% of the water depth, near each boundary, and decreased tenfold over the mixed layer extent (Fig. 5a). SML and BML ϵ were log-normally distributed, log-averaging to $2.9 \times 10^{-8}\,\mathrm{W\,kg^{-1}}$ and $3.8 \times 10^{-8}\,\mathrm{W\,kg^{-1}}$, respectively. Approximately 26% (SML) and 27% (BML) of observations had elevated to strong dissipation $\epsilon > 10^{-7}\,\mathrm{W\,kg^{-1}}$ (Fig. 5b). Moderate to weak stratification was found in the SML, averaging to $N^2 = 3.6 \times 10^{-7}\,\mathrm{s^{-2}}$ and
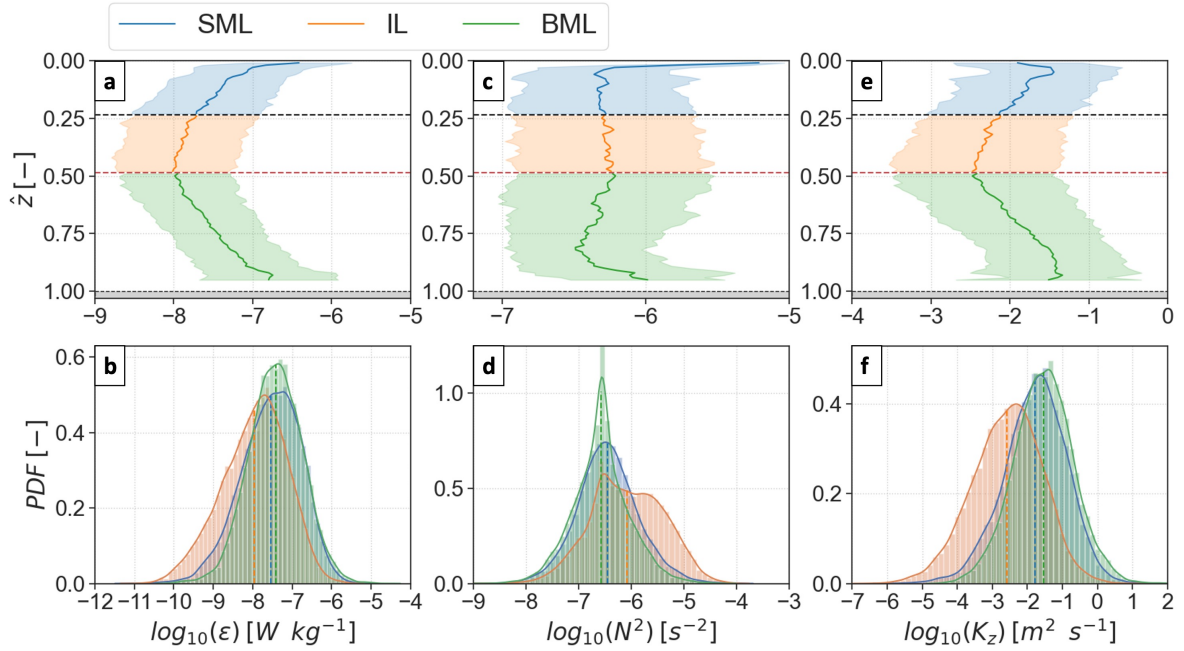
Figure 5. Log-averaged profiles along normalised water depth ($\hat{z}$, top row) and probability density function (PDF, bottom row) of (a)-(b) dissipation rates, (c)-(d) buoyancy frequency squared and (e)-(f) diapycnal diffusivity. In the top row, time-averaged mixed layer extents are represented. The time-averaged top (black dashed line) and bottom (red dashed line) depths of the interior layer (IL, green), delineate indicatively the mean surface (SML, blue) and bottom (BML, green) mixed layers. Dark lines indicate the mean values and the lighter envelope show the ± 1 standard deviation intervals. In the bottom row, the SML, IL and BML subsets are made of the instantaneous points for each glider profile. Solid lines indicate the curve fit of the underlying lighter coloured histograms, and the dashed lines the mean value of each distribution.

increasing near the surface to elevated values in normalised water depths ($\hat{z}$) below 0.05 (Fig. 5c). Stratification depth-bin averages in the BML were weaker overall and varied more significantly, with a narrower distribution around a $2.7 \times 10^{-7}\,\mathrm{s}^{-2}$
275   mean (Fig. 5d). As a result, elevated to strong diffusivity (log-mean $K_z > 10^{-2}\,\mathrm{m}^2\,\mathrm{s}^{-1}$) was found in the upper and lower 25% of the water column (Fig. 5e).

Diapycnal diffusivity distributions were log-normal in both mixed layers, but with a BML log-mean (mean) of $3 \times 10^{-2}\,\mathrm{m}^2\,\mathrm{s}^{-1}$ ($0.3\,\mathrm{m}^2\,\mathrm{s}^{-1}$), twice higher than in the SML, as N^2 was lower overall (Fig. 5f). 70% and 60% of SML and BML samples were elevated to strong ($K_z > 10^{-2}\,\mathrm{m}^2\,\mathrm{s}^{-1}$), much higher than in the interior layer (30%), as N^2 was on average $2-3$ times higher
280   than in the mixed layers.

Table 2. Characteristics of interior turbulence interactions and mixed layer overlapping: duration (Span) and ranges of along-shore current (V) and wind ($Wind$) speeds, interior layer thickness (δ_{IL}), dissipation rate (ϵ), stratification (N^2) and diapycnal diffusivity (K_z). The ranges of ϵ are scaled by $\epsilon_p = 3 \times 10^{-9}\,\mathrm{W\,kg^{-1}}$, the criteria for identifying interior turbulence interactions (see details in text). * markers indicate episodes that are moreover associated with mixed layer overlapping (black rectangles in Fig. 4).

	Span	V	$Wind$	δ_{IL}	ϵ/ϵ_p	N^2	K_z
	[h]	[m s^{-1}]	[m s^{-1}]	[m]	[−]	$\times 10^{-4}$ [s^{-2}]	$\times 10^{-5}$ [m^2 s^{-1}]
i	3	-0.6 - 0.4	2 - 4	25 - 31	1 - 10^2	5×10^{-3} - 0.8	1 - 10^4
ii	6	-1.2 - 0.8	10 - 14	19 - 77	7 - 10^3	3×10^{-4} - 0.8	9 - 3×10^4
iii*	4	-0.8 - 1.2	10 - 13	-	15 - 7×10^2	10^{-4} - 0.05	20 - 3×10^5
iv	4	-0.6 - 0.8	13 - 15	47 - 110	1 - 10^3	2×10^{-4} - 0.3	7 - 3×10^4
v	3.5	-0.2 - 1	12 - 15	46 - 108	1 - 7×10^2	2×10^{-4} - 1	10 - 2×10^4
vi*	4.5	-0.4 - 1.2	9 - 14	-	1 - 10^3	1×10^{-4} - 0.2	70 - 7×10^5
vii*	2	-0.4 - 1.2	10 - 14	-	1 - 7×10^2	9×10^{-5} - 0.06	80 - 3×10^5
viii	2.5	0 - 0.8	4 - 7	15 - 74	1 - 30	2×10^{-4} - 0.08	20 - 7×10^3
ix	3	-0.4 - 0.6	7 - 11	17 - 100	1 - 70	1×10^{-4} - 0.05	5 - 7×10^4
x	1.5	-0.6 - 0.2	6 - 7	22 - 55	3 - 70	4×10^{-4} - 0.09	3 - 2×10^4

3.3 Overlapping mixed layers and interior turbulence interactions

Three overlapping mixed layers episodes were observed, when mid-water column diapycnal diffusivity was strongly-enhanced (Fig. 4). Background stratification was moderate to weak during overlapping episodes, peaking at $2 \times 10^{-5}\,\mathrm{s^{-2}}$ during episode vi and otherwise reduced by $3 - 4$ orders of magnitude (Table 2). Dissipation increased to $100 - 1000 \times \epsilon_p$ throughout the water depth. This yielded strongly-enhanced mid-water column diapycnal diffusivity, *a minima* $2 \times 10^{-4}\,\mathrm{m^2\,s^{-1}}$, and enhanced by $4 - 5$ orders of magnitude to peak at $20\,\mathrm{m^2\,s^{-1}}$. For context, mean K_z reached $4 \times 10^{-2}\,\mathrm{m^2\,s^{-1}}$ in Gibraltar strait, the canonical strait at this scale (Wesson and Gregg, 1994; Stevens, 2018), and $3 \times 10^{-5}\,\mathrm{m^2\,s^{-1}}$ for the upper-1000 m global ocean (Waterhouse et al., 2014).

The mixed layers overlapped during periods of elevated tidal and wind forcing, destabilizing the variable interior stratification (Table 2). Sustained wind speeds ranging in $9 - 14\,\mathrm{m\,s^{-1}}$ combined with fast flow speeds in $-0.8 - 1.2\,\mathrm{m\,s^{-1}}$ during episodes iii, vi-vii. Episodes iii, vi also occurred during enhanced bottom shear periods, reaching $3.9 \times 10^{-6}\,\mathrm{s^{-2}}$ (see Section 3.1). Although boundary forcing conditions and full enhancement of water depth diffusivity were found to be similar during episodes iii, vi-vii, the previous stratification configurations differed significantly (Fig. 4). The depth of the SML was $\sim 40\,\mathrm{m}$ before episode iii, compared to $80 - 100\,\mathrm{m}$ before episodes vi-vii. BML depth extended to $30 - 50\,\mathrm{m}$ above the seabed before episodes iii,vi, compared to $\sim 100\,\mathrm{m}$ before episode vii. Furthermore, while the interior stratification was mostly elevated to strong ($N^2 > 10^{-6}\,\mathrm{s^{-2}}$) prior to episodes iii and vi, it was moderate to weak before episode vii.

Interior turbulence interactions outside mixed layer overlapping episodes were also observed (Table 2). During episodes i-ii, iv-v, viii-x, dissipation increased to $100 - 1000 \times \epsilon_p$ throughout the water depth, similarly to mixed layer overlapping, with an interior layer thickness reduced $\sim$threefold from the mean. Stratification was slightly stronger than during overlapping mixed
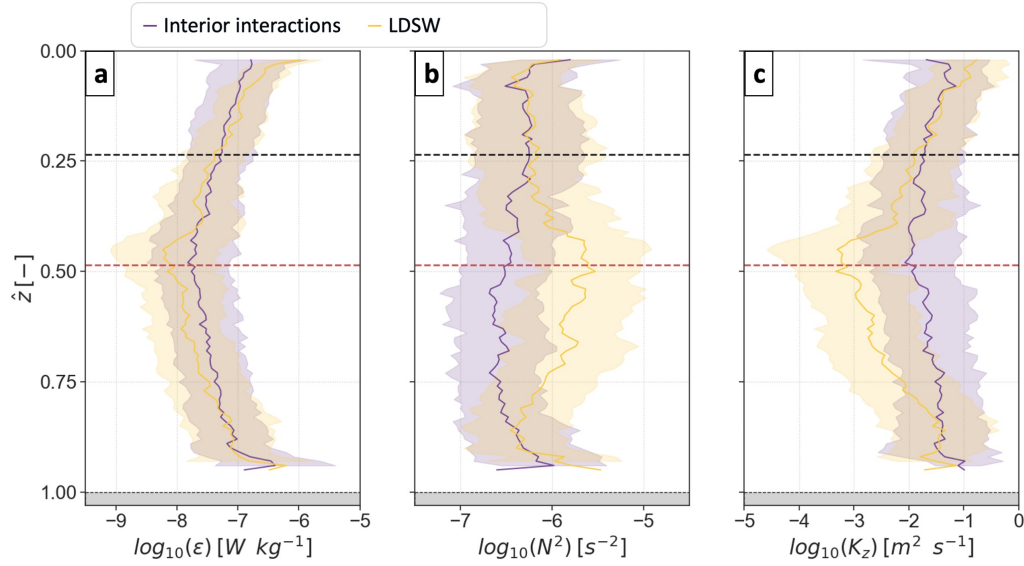
Figure 6. Average profiles with normalised depth ($\hat{z}$) of observations of (a) dissipation rates, (b) buoyancy frequency squared and (c) canonical diffusivity during interior interactions (purple) and low density surface waters (LDSW, yellow) periods (see Fig. 4a). In all panels, dark lines indicate the log-averages and the lighter envelopes show ± 1 standard deviation. The mean surface (SML) and bottom (BML) mixed layer depths are indicated with black and red dashed lines, respectively.

300 layer episodes iii, vi-vii, leading to $3-4$ orders of magnitude increase in interior K_z compared to $4-5$. This notably led to mixed layer overlapping during episode iii but not episode ii where similar flow and wind speeds were found. In general, flow speeds were slower during episodes i-ii, iv-v, viii-x, and wind speeds ranged in $2-15\,\mathrm{m\,s^{-1}}$.

Interior turbulence interactions, including mixed layer overlapping, enhanced vertical diffusivity 20-30 fold, on average, from the baseline configuration where low density surface waters isolate bottom and surface turbulence (Fig. 6). To quantify
305 the bulk impact of interior turbulence interactions, profiles of ϵ, N^2 and K_z over a period of four tidal cycles are averaged in two subsets: during or outside of the baseline low-density-surface-waters (LDSW hereafter) configuration (see Fig. 4a). The latter includes episodes ii-vii of interior turbulence interactions, containing the three mixed layer overlapping (iii, vi and vii) episodes. For $0.25 < \hat{z} < 0.8$, LDSW ϵ was twofold weaker, N^2 fourfold stronger, translating to 7 times weaker K_z. The largest difference was found at the mean interface depth of BML and interior layer ($0.45 < \hat{z} < 0.55$) with a $20-30$ fold
310 increase in K_z during episodes of interior turbulence interactions and mixed layer overlapping (Fig. 6). Across $\pm 30\,\mathrm{m}$ around the mean depth of the interior layer base ($\hat{z} = 0.485$), diapycnal diffusivity averaged (log-averaged) to 0.12 (0.07) and 0.04 (0.01) $\mathrm{m^2\,s^{-1}}$ for interior interactions and LDSW episodes, respectively.

The canonical diapycnal diffusivity ($K_z(\Gamma = 0.2)$) results above, from high-turbulence generated primarily in the mixed layers, are discussed in the framework of boundary-limitation of overturning scales and parameterization of diapycnal diffusivity
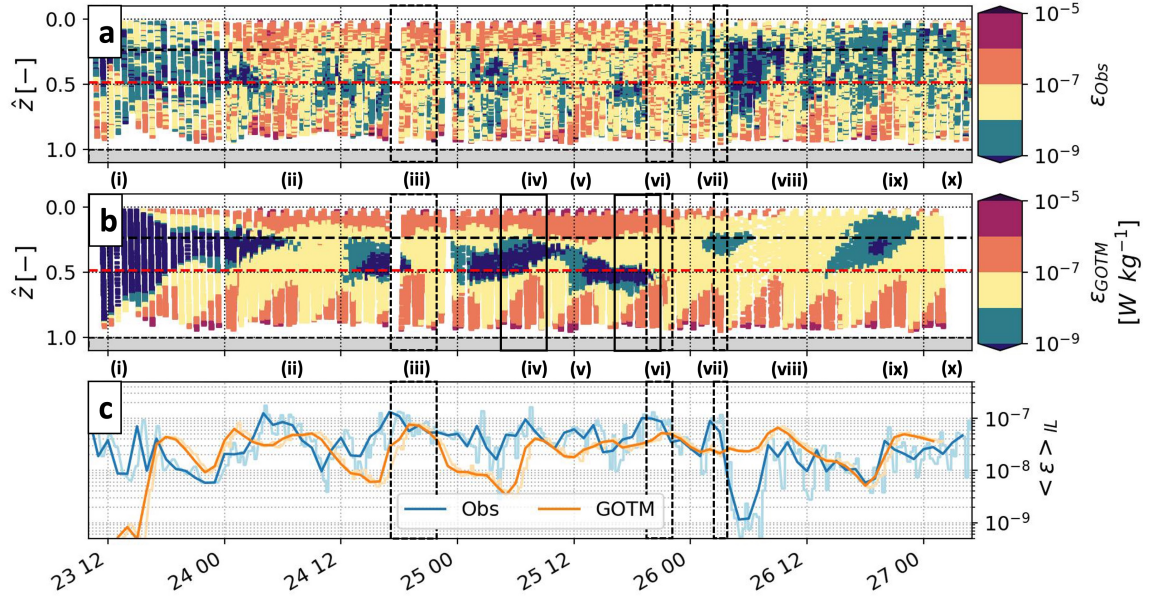
Figure 7. Normalised depth-time series of dissipation rates from (a) microstructure observations (ϵ_{Obs}); (b) GOTM estimates interpolated on the microstructure profile depths (ϵ_{GOTM}); (c) depth-averages over the mean interior layer extent ($\langle \epsilon \rangle_{IL}$) of observations (blue) compared to GOTM estimates (orange). In panels (a-b) the mean surface (SML) and bottom (BML) mixed layer depths are indicated with black and red dashed lines, respectively. For all panels, episodes of interior turbulence interactions are numbered (i-x) and the instances when mixed layers overlap episodes are marked with black dashed rectangles. The two solid black rectangles in panel (b) highlight case 1 (isolated boundary turbulence) and 2 (interacting boundary turbulence) time periods used in Section 4.3.

315   ($K_z(\Gamma = f(Re_b))$) in Section 4.2. The implications for biophysical processes in the coastal ocean, of K_z modulation when boundary layer turbulence overcomes transient stratification and overlaps in the interior, are discussed in Section 4.4.

3.4   Comparison with modelled turbulence

The vertical structure of ϵ in Te-Moana-o-Raukawa/Cook Strait was primarily modulated by three external factors: winds, tides and transient stratification. To evaluate the interaction of turbulent kinetic energy mechanisms that generate the observed ϵ

320   structure, observations were compared to one-dimensional turbulence modeling outputs. GOTM was prescribed with simplified but realistic boundary forcing (wind stress time series and monochromatic M_2 tides, Section 2.4) and transient stratification (relaxation to T-S observations, Section 2.4). The vertical temperature structure was prescribed from glider observations and GOTM was used to understand the interior interactions and changes in turbulent kinetic energy structure.

   GOTM captured key aspects of the magnitude, vertical structure and interior interactions of ϵ observations (Fig. 7). Mod-

325   elled surface dissipation was within an order of magnitude of observations, except during weak wind-forcing when systematic

overestimation was found (e.g., 23 June, Fig. 7a-b). Modelled bottom dissipation was also within an order of magnitude of observations, with the largest differences near the seabed in the intervals between enhanced ϵ pulses. The vertical ϵ structure in the mixed layers was well represented in the model, although vertical ϵ propagation away from the boundaries was largely underestimated. In general, the frequency of interior turbulence interactions was underestimated in GOTM, although interior magnitudes were reasonably represented (Fig. 7c). Interior turbulence interactions (e.g. episode ii) and boundary layer overlapping (e.g. episodes iii and vi) were too slowly established in the model, or not at all (e.g. episodes iv-v, ix), when the vertical extent of enhanced surface (e.g. episodes ii-iii) or bottom (e.g. episodes iii-v, ix)-driven dissipation was underestimated in the model.

4 Discussion

Autonomous glider observations of turbulence in a weakly-stratified, energetic coastal sea captured the interactions and overlap of surface and bottom mixed layers. During a four-day, high wind and spring tide period, diffusivity within the respective mixed layers was enhanced. There were ten interior turbulence interactions, including three occurrences when the mixed layers overlapped, and interior diapycnal diffusivity intensified 20-30 fold. In Section 4.1, we discuss the turbulence processes at play in the mixed layers and why they overlap. In Section 4.2, we discuss the sensitivity of the overlap observations to methodological choices. In Section 4.3, we discuss the sources and sinks of turbulence and their relation to the overlapping process. In Section 4.4, we discuss the potential implications for coastal seas mixing dynamics.

4.1 Turbulence in the mixed layers

In the BML, ϵ was highest, log-averaging to $\epsilon = 2.2 \times 10^{-7} \, \mathrm{W\,kg^{-1}}$ closest to the seabed. Bottom dissipation coincided with periods of enhanced vertical shear (Fig. 8a,c). Weaker ϵ in the upper BML was an order of magnitude smaller and, in general, dissipation in the BML was inversely related to vertical shear. On average, ϵ levels in the upper BML ($0.5 < \hat{z} < 0.6$) were weaker during maximum than minimum shear periods, increasing by an order of magnitude to $\epsilon = 2.2 \times 10^{-7} \, \mathrm{W\,kg^{-1}}$ (3.4 times higher than for the minimum shear periods) closest to the seabed.

The presence of four bottom-generated ϵ pulses daily is usual at sites where M2 barotropic tides control turbulence generation (Wang et al., 2014; Schultze et al., 2017; Becherer et al., 2022). Enhanced ϵ propagated upward to $\sim 80\,\mathrm{m}$ above the seabed in $4-4.5\,\mathrm{h}$ yielding an approximate vertical speed of $5 \times 10^{-3}\,\mathrm{m\,s^{-1}}$ (see e.g., episodes v, viii in Fig. 4), of the same order of magnitude as ϵ observations driven by $\sim 1\,\mathrm{m\,s^{-1}}$ tidal forcing in a weakly stratified shelf sea (Thorpe et al., 2008). The ϵ envelope for a pulse generated close to the wall during the acceleration phase reached its maximal height above bottom after $4-4.5\,\mathrm{h}$ of the deceleration phase. Large Eddy Simulations of oscillatory current-driven turbulence in a stratified boundary layer (Gayen et al., 2010) matches the ϵ dynamics of tidal phases in Cook Strait. Stratification adjacent to the bottom mixed layer modulated the upward extension of bottom-generated turbulence, akin to observations (Wang et al., 2014) and simulations (Gayen et al., 2010) elsewhere.
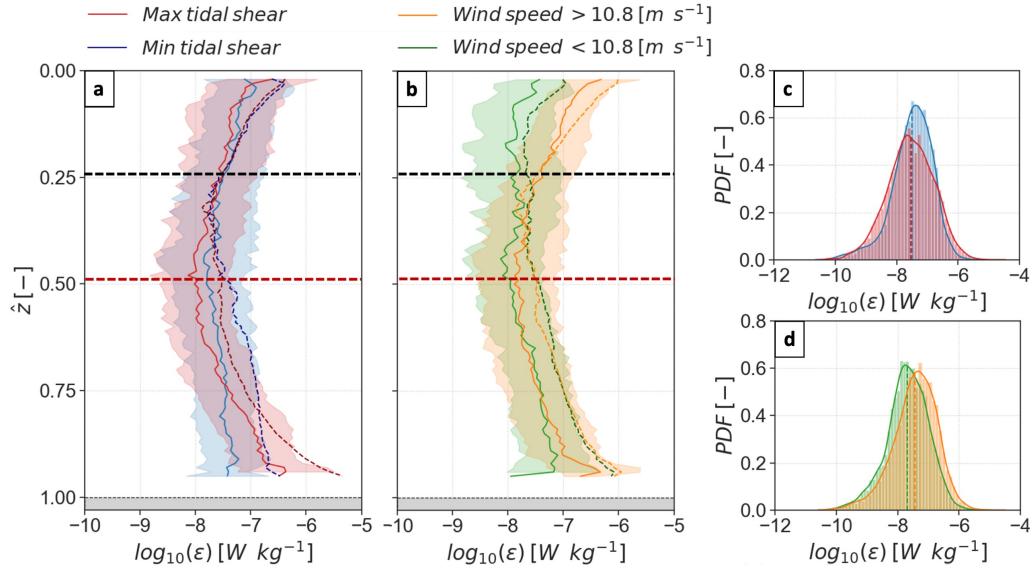
Figure 8. The vertical structure of dissipation rates, during periods of varying tidal shear and wind speeds, are presented here and used to validate GOTM results. Log-averaged profiles along normalised depth ($\hat{z}$) of dissipation rates from the observations (light-colored continuous lines, with ± 1 log-standard deviation interval shaded), and GOTM estimates (dark-colored dashed lines) for regimes of (a) maximal (red) or minimal (blue) tidal shear and (b) high (orange) and low (green) winds (see Section 3.1 and Fig. 4a). Associated probability density function (PDF) of each tidal-shear and wind averaging-periods of observed ϵ are shown in (c) and (d), respectively. In panels (a-b) the mean surface (SML) and bottom (BML) mixed layer depths are indicated with black and red dashed lines, respectively.

Strong winds elevated dissipation in the SML (Fig. 8b,d) and the ϵ log-mean increased up to twentyfold from the low-wind conditions. Elevated winds did not always induce overlapping mixed layers, however ϵ in the interior layer increased two-fold compared to low wind conditions. The depth and magnitude to which ϵ was enhanced are consistent with high wind-driven mixing in shelf seas of various depth-ranges (MacKinnon and Gregg, 2005; Williams et al., 2013; Schultze et al., 2020).

When the SML and BML overlapped, interior ϵ increased by three orders of magnitude from the ϵ_p baseline (Table 2). Mid-water depth log-averages were four-times greater than during the more strongly stratified LDSW conditions. (Fig. 6). Generally, interior ϵ was of the same order of magnitude (or less) than the near-boundary levels (Fig. 4d). This was also true during SML and BML overlapping. Suggesting that in these Te-Moana-o-Raukawa/Cook Strait observations, boundary-generated turbulence combined linearly in the interior. This might indicate that the boundary-generated turbulence, although originating from non-linear sources, can appear as a linear response of the mean shear flow (Landahl, 1988, 1989; Jiménez, 2013). As such, the observations did not show that boundary-generated turbulence interacted with interior stratification to produce turbulence via internal wave generation and breaking (Gayen et al., 2010; Zhang and Tian, 2014; Wang et al., 2014).

An interior region of approximately $\sim 50\,\mathrm{m}$ had moderate-elevated ϵ in the $2\,\mathrm{h}$ preceding the mixed layer overlapping epsisode vi (Fig. 4d). This notable occurrence appeared to be linked to a detached burst of turbulence from the strong BML

pulse of episode v, rising at $2-5\,\mathrm{m\,s^{-1}}$. With a certain degree of vertical spreading, it is akin to the BML burst ejection mechanism described in Thorpe et al. (2008). Albeit of weaker ϵ, this pattern of burst ejection outside of the BML was observed two more times. All three occurrences happened during particularly deep and strong stratification configurations in the water column. If the bulk interior stratified layer sits within the bulge of high turbulence tidal pulses, a portion of the bottom-generated turbulence can be suppressed and high-ϵ bursts can detach and travel upward in the water column (Thorpe et al., 2008). Similar ejection mechanisms can affect sediment transport processes in bottom boundary layers (Li et al., 2022; Wu et al., 2022).

The two main overlapping episodes iii and vi were of similar duration, forcing speeds and turbulence characteristics (Table 2), however initial conditions were different (Fig. 4). In the $2-3\,\mathrm{h}$ prior to either episode, surface and bottom-driven elevated-strong ϵ were co-located in time with a thick ($>50\,\mathrm{m}$) and elevated-strong interior stratification (Fig. 4c,d). In both cases, the BML depth was relatively deep, within $50\,\mathrm{m}$ of the seabed. The SML depth was approximately twice as thick before vi, but enhanced surface ϵ extended deeper ahead of the episode iii overlapping event. Similar strength in stratification occurred near the seabed but the bottom-driven turbulence of episode iii appeared to be strong enough to destabilise stratification and connect with surface-driven ϵ during the decelerating tidal phase. This is different to episode vi, which is characterised by a more distinctive BML ϵ pulse. For this episode, the overlapping mechanism was initiated by turbulence present in the mid-water column, most likely* a burst ejected from the BML during episode v (Thorpe et al., 2008).

Interior turbulence interactions were also identified in the results, representing mixing layer overlapping (see Section 3.3 and Figure A1). Mixing layers portray active mixing, referring to a different timescale than the mixed layer, which illustrates the history of mixing (Sutherland et al., 2014; Giunta and Ward, 2022). Periods when mixing layers overlap but mixed layers do not (events i-ii, vi-v, viii-x) thus indicate vigorous mixing activity and enhanced vertical turbulence exchanges (see Section 4.3) that fail to bring interior tracers, e.g. here temperature, to homogeneity. Differences between mixed and mixing layer overlapping attest to the myriad of dynamical surface of bottom boundary layer processes that affect turbulence generation and the stratification it works against, e.g., surface-driven restratification allowing for a shallower SML than surface mixing layer (Sutherland et al., 2014; Esters et al., 2018).

The presence of mixed layer overlapping events were compared to bulk metrics for stratified systems (Fig. 9). For a depth-integrated metric, the pulses of dissipation enhancement generally match well-mixed conditions, where $log_{10}(H/u^3)$, the Simpson-Hunter stratification index, is below the commonly-used $2.7-3$ critical range (Simpson and Hunter, 1974; Marsh et al., 2015; Timko et al., 2019). Applying the bulk formulation of a Cook Strait stratification study by Bowman et al. (1983), depth-integrated ϵ variations match conditions where the majority of the work to mix the water column (ϕ/H, potential energy deficit per unit volume) would be attributed to tidal kinetic energy dissipation (Fig. 9a). The short-lived nature of mixed layer overlapping is difficult to distinguish using bulk metrics. For example, events vi-vii were not associated with high tidal energy dissipation ($ku^3/\phi < 30\%$) before or during the events. The contribution of surface buoyancy fluxes to bulk stratification ($\bar{b}H/u^3$) can be noted only before and during events ii-vi, indicating only a minor contribution to restratification processes (Fig. 9b). While, broadly, some of the turbulence and mixed layer overlapping characteristics can be resolved by variations in these bulk metrics, much more complexity is at play when mixed boundary layers overlap.
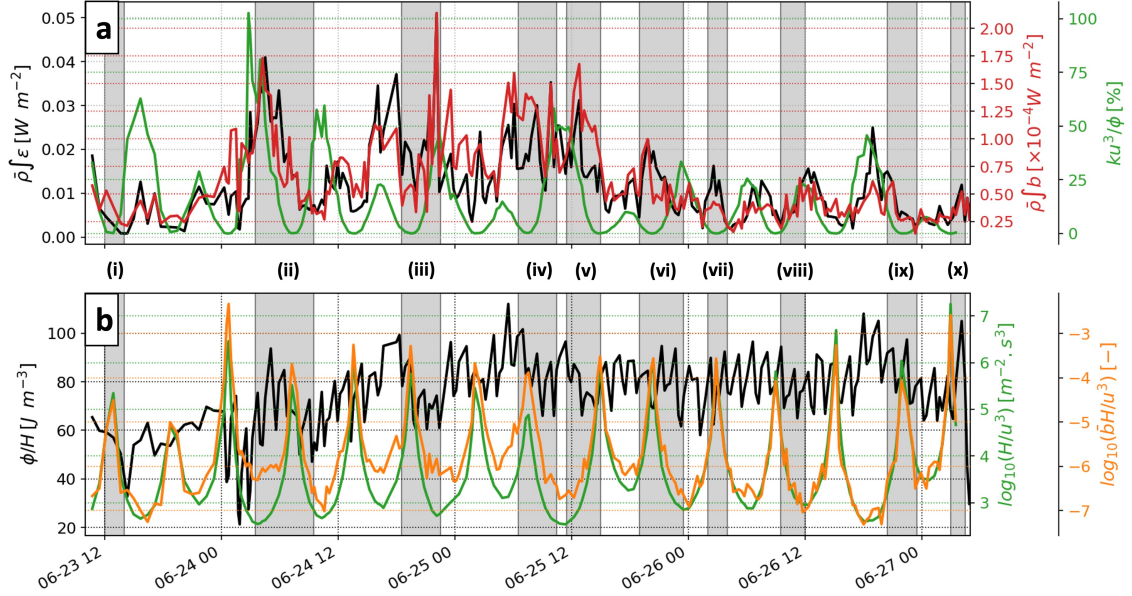
Figure 9. Depth-integrated metrics provide background to events of interior turbulence interactions and mixed layer overlapping. (a) Observed depth-integrated dissipation rates and buoyancy flux (b, see Figure A2a), contextualised with a simple model for the proportion of work needed to mix the water column attributed to tidal kinetic energy (ku^3/ϕ, see details in text). (b) Observed work required to mix the water column (ϕ/H, also called potential energy deficit) contextualised with the Simpson-Hunter model for stratification (H/u^3) and the non-dimensional contribution of mean surface buoyancy flux to bulk stratification ($\bar{b}H/u^3$, with $\bar{b}$ denoting the $0-50\,\text{m}$ average). Episodes of interior turbulence interactions are highlighted with light grey rectangles and numbered (i-x).

4.2 Sensitivity to stratified turbulence observing methods

Estimating background stratification, N^2, remains a source of uncertainty for the application of Equation 1, the Osborn formula (Gregg et al., 2018; Arthur et al., 2017). In the observations, adiabatically-rearranged (i.e. sorted) vertical density profiles were used to compute a statically stable background stratification, i.e. $N^2 > 0$ (Thorpe and Deacon, 1977; Mater et al., 2015). In the GOTM simulations, N^2 is computed internally using the prescribed, raw, glider-based T and S profiles (see Section 2.4). Convective adjustment subroutines are used in GOTM to control static stability, however, $N^2 < 0$ is allowed (Umlauf et al., 2012).

Positive values of the buoyancy flux, G, were output by GOTM, as raw, un-sorted, temperature and salinity observations were prescribed to the model (see further discussion of model sensitivity to observation interpolation in Section 4.3). Albeit of secondary importance relative to shear production, $G > 0$ values can be of similar magnitude as T_k in some portions of the boundary layers (Fig. 11 and A3). Sign indefinite G represents the reversibility of potential and kinetic energy exchanges during turbulent mixing episodes, identified as a source of uncertainty when quantifying irreversible mixing processes (Caulfield,
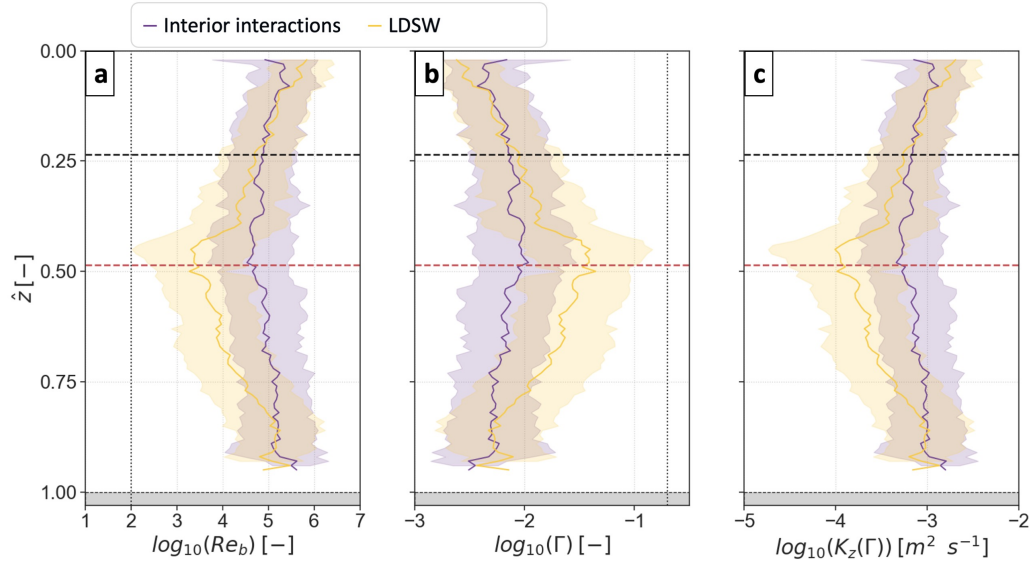
Figure 10. Elevated levels of turbulence activity lead to parameterised mixing efficiency and diapycnal diffusivity reduced hundredfold compared to canonical values. Average profiles with normalised depth ($\hat{z}$) of observations of (a) buoyancy Reynolds number, (b) mixing efficiency coefficient and (c) diffusivity with a variable mixing efficiency coefficient, during interior interactions (purple) and low density surface waters (LDSW, yellow) periods (see Fig. 4a). In all panels, dark lines indicate the log-averages and the lighter envelopes show ± 1 standard deviation. The mean surface (SML) and bottom (BML) mixed layer depths are indicated with black and red dashed lines, respectively. In panels (a,b), the dotted black vertical lines indicate the $Re_b = 100$ threshold for isotropic turbulent motions and the canonical $\Gamma = 0.2$ value for mixing efficiency, respectively.

2020). Thus, using adiabatically-rearranged density could lead to some overestimation of the proportion of TKE dissipation that drives irreversible mixing and enhances diapycnal diffusivity (Eq. 1).

420 The use of a constant mixing efficiency coefficient, i.e. $\Gamma = 0.2$, potentially overestimates diapycnal diffusivity of weakly-stratified and energetic turbulence (Bluteau et al., 2017; Monismith et al., 2018). This is especially relevant to homogeneous, shear-driven turbulence, such as is expected in strongly-forced boundary layer flows, where boundary proximity can limit the growth of turbulent eddies (Shih et al., 2005; Holleman et al., 2016; Monismith et al., 2018). Due to the elevated boundary-driven turbulence observed in Te-Moana-o-Raukawa/Cook Strait, differences between using $\Gamma = 0.2$ or a buoyancy Reynolds

425 number-based parametrization to quantify diapycnal diffusivity are evaluated. The Bouffard and Boegman (2013) parameter-ization is used here, supported by a range of modeling, field and laboratory measurements of high-turbulence Γ (Barry et al., 2001; Shih et al., 2005; Monismith et al., 2018). For the complete time-series, the mean diffusivity for parameterised K_z was $9 \times 10^{-4}\,\mathrm{m^2\,s^{-1}}$, while the mean canonical K_z was $0.1\,\mathrm{m^2\,s^{-1}}$. As such, the bulk difference was of two orders of magnitude, with the mean parameterised K_z being 0.9% of the canonical K_z. Further, the variable Γ modulates the overall K_z structure

430 through the SML and BML. Parameterised log-mean Γ values can be up to 60 times reduced from 0.2 near the boundaries, and
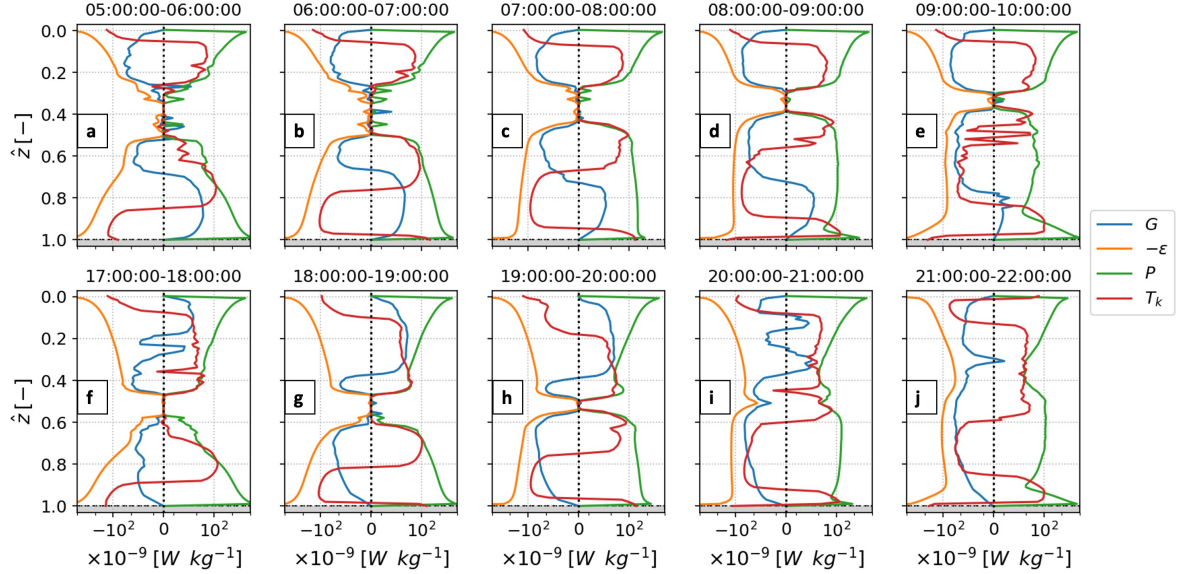
Figure 11. Shear-driven turbulent kinetic energy produced near the boundaries can interact in the interior, when vertical transport is enhanced. Normalised hourly averaged profiles of GOTM estimates of TKE source (> 0) and sink (< 0) terms of Eq. 3 for (a-e, case 1) isolated or (f-j, case 2) interacting turbulent layers. Buoyancy flux (blue), dissipation rate (orange), shear production (green) and vertical transport (red) of TKE are shown. The continuous and dashed line for $-\epsilon$ represent where ϵ is higher or lower than ϵ_p, respectively.

up to 20 and 4-fold at the mean interior layer base ($0.45 < \hat{z} < 0.5$) during LDSW and interior turbulence interactions episodes, respectively. This lead to a five-fold increase in $K_z(\Gamma)$ during interior turbulence interactions episodes, compared to $20 - 30$ fold for $K_z(\Gamma = 0.2)$ (Fig. 6). In the $\pm 30\,\mathrm{m}$ around $\hat{z} = 0.48$, the mean interior layer base, mean (log-mean) $K_z(\Gamma)$ levels are 5×10^{-4} (3×10^{-4}) and 1×10^{-3} (1×10^{-3}) $\mathrm{m^2\,s^{-1}}$ for interior turbulence interactions and LDSW episodes, respectively.

435 Interior turbulence interactions enhance mean (log-mean) diffusivity by two (three)-fold, compared to three (seven)-fold for $K_z(\Gamma = 0.2)$ at the interior mixed layer boundaries (Fig. 6). At the interior mixed layer boundary, mean parameterised K_z was elevated to $1 \times 10^{-4}\,\mathrm{m^2\,s^{-1}}$ during overlapping, only 0.5% of the corresponding mean $K_z(\Gamma = 0.2)$. Using an arguably more realistic scaling for Γ, interior turbulence interactions, including mixed layer overlapping, enhance diapycnal diffusivity, albeit at weaker K_z than using a constant coefficient.

440 ### 4.3 Sources and sinks of interior turbulence

Understanding the mechanisms which led to isolated (case 1) or interacting boundary-driven turbulence (case 2) were examined using GOTM-based hourly averages of TKE source (> 0) and sink (< 0) terms of Eq. 3 (Fig. 11). The turbulent boundary layers were defined using the same threshold criteria that was applied to OMG observations to detect interior turbulence interactions,

analogous to mixing layer overlapping (Section 2.2, see also Figure A1). In both cases, turbulent boundary layers where
shear production and dissipation are the dominant source and sink of TKE, respectively, grow through entrainment against the
stabilizing interior stratification that inhibits vertical turbulent exchanges (Gayen et al., 2010; Yan et al., 2022).

Case 1 and 2 are initially forced by similar wind strength (in $10-15\,\mathrm{m\,s}^{-1}$) and tidal flows, but differ in upper water column
stratification and turbulent surface layer extent (Fig. 2, 4c). Both cases showed similar depth-extent of bottom turbulence, but
surface turbulence extended deeper for case 2 (see Fig. 11a,f). In both cases, "vertical transport", T_k, is a near-boundary TKE
sink of secondary importance ($1-2$ orders of magnitude lower than ϵ) and a primary TKE source (comparable magnitude
to P) in the turbulent boundary layers. Kinetic energy transfer from the boundaries towards the interior was confined in the
respective turbulent layers, since $T_k \rightarrow 0$ in the interior (Yan et al., 2022; Becherer et al., 2022).

During subsequent stages, when the wind forcing remains strong and the tidal forcing enters the deceleration phase, the tur-
bulent bottom layer grows in both cases, but the turbulent surface layer only significantly deepens in the interacting boundary-
driven turbulence scenario of case 2 (Fig. 11b-e,g-h). The shallow transient stratification of case 1 was strong enough to
dampen T_k and impede surface layer growth, isolating the turbulent layers. The turbulent layers remain isolated even though
high source levels (primarily P and T_k) are observed in the bottom layer and especially in the deep edge of the interior
separation (Fig. 11b-e).

In case 2, high levels of T_k (comparable to P) at both edges of the interior separation successfully provides the TKE source
that supports the gradual pycnocline erosion from above and below (Yan et al., 2022; Becherer et al., 2022) during a transition
phase (Fig. 11g-h) until the layers overlap (Fig. 11i-j). T_k fully connects in the interior when turbulent layers fully overlap, due
to the slow reduction of interior stratification rather than boundary layer growth, as suggested in Yan et al. (2022). T_k further
represents the vertical divergence of the TKE flux, which has been shown to be a significant source of deviation from local
TKE balance (Scully et al., 2011). Whether T_k directly contributes to stratification erosion or indirectly as a contributor to
dissipation-driven mixing was not ascertained here. Nevertheless, this process appears to dominate. Six out of the ten interior
turbulence interaction events, including the three ML overlapping, show similar T_k structure and interplay of TKE terms
(Figure A3). T_k in the interior is in parts of comparable magnitude with local shear production, also near the boundaries as
another phase of enhanced tidal shear starts and wind fluctuates (Fig. 2). Overall, dissipation is driven up by two orders of
magnitude in the mid-water column.

The primary difference between cases 1 and 2 is in the initial turbulent surface layer extent, a balance of wind-driven
turbulence against interior stratification for the examples chosen here. In $\mathcal{O}(200\,\mathrm{m})$-deep tidally-forced systems, turbulent
boundary layer overlapping occurs when winds are high enough and interior stratification fluctuates. Giving echo to Yan et al.
(2022) insights where Langmuir super-cell turbulence is theorised to drive boundary layer overlapping, albeit in much shallower
systems.

The buoyancy flux (G) is a TKE sink for most of the water column for both cases but a source near the surface (case 2)
or the bottom (case 1) boundary. Although of negligible magnitude against primary TKE terms in Eq. 3, intermittent $G > 0$
spikes are of comparable amplitude to P spikes found in the interior during the initial stage of case 1 (see Fig. 11a-b). The
contribution of buoyancy fluxes to turbulence production thus appears non-essential to the overlapping process. It contributed

however to the interior turbulence interactions of event viii, as G was above $10^{-9}\,\mathrm{W\,kg}^{-1}$ across the water depth (Figure A3d). To note, further processing of observation interpolation, e.g. sorting T-S observations and increasing the relaxation time-scale, do reduce $G > 0$ occurrences and magnitude (not shown). These cases however cause a significant deviation of the other TKE terms from the GOTM results presented here, which showed to portray best the direct OMG observations of ϵ structure and boundary layer interactions.

Winds and tides consistently shape the vertical structure of dissipation in the GOTM regime averages (Fig. 8). While the ϵ structure of enhanced boundary forcing in GOTM broadly matched observations, the depth away from boundary of log-mean ϵ increased during periods of enhanced tidal shear (Fig. 8a) or wind speed (Fig. 8b) forcing was underestimated in the model. As a consequence, several episodes of interior turbulence interactions in the observations were misrepresented in the GOTM results, as shown, for example, in Fig. 7 where mean levels of the interior layer ϵ were underestimated (for example, episodes iv and vii) or overestimated (for example, episodes viii and ix). The former could originate in the underestimation of either surface (iv) or bottom (vii) turbulence transfer to the interior, while the latter could be an indication of lateral transport of turbulence.

4.4 Implications of overlapping boundary layers in coastal seas

Varying stratification and forcing in shelf seas compete to enable interior turbulence interactions and enhanced diffusivity. Although Te-Moana-o-Raukawa/Cook Strait has been classified as weakly-stratified (Stevens, 2014, 2018), in this study transient stratification opposed interior turbulence interactions and mixed layer overlapping, with a bulk order-of-magnitude difference (Fig. 6). Further, bulk stratification, $log_{10}(H/u^3)$, ranged in $2.3 - 7.4\,\mathrm{s}^3\,\mathrm{m}^{-2}$ (Fig. 9b), consistently with if not more strongly stratified than other Te-Moana-o-Raukawa studies (Bowman et al., 1983) and shelf seas of similar depths (Garrett et al., 1978; Marsh et al., 2015). Restratifying surface buoyancy fluxes scaled to bulk stratification, $log_{10}(\bar{b}H/u^3)$, averaged to -4.3, suggesting a similar influence than in much shallower estuarine systems (Ralston et al., 2010; Orton et al., 2010). This indicates that if it were not for the transient stratification influx at the base of the warm surface waters, from water masses advected through the strait, and to a minor extent restratification from buoyancy fluxes, interior turbulence interactions and full-water column turbulence would have occurred at tidal frequency during the high winds period.

Horizontal variability at submesoscales in Greater Te Moana-o-Raukawa/Cook Strait influences transient stratification. Evidence of a SST front advected $\sim 40\,\mathrm{km}$ south during 25-27 June is shown here (Fig. 3). At the submesoscale in Greater Te Moana-o-Raukawa/Cook Strait, SML baroclinic instabilities and fronts of typical length scale $0.1 - 1.6\,\mathrm{km}$ can have an advection timescale of $0.2 - 8\,\mathrm{h}$ (Jhugroo et al., 2020), comparable to the $6\,\mathrm{h}$ period of tidal generation of BML in a strait. These features have been shown to strengthen vertical stratification to $\mathcal{O}(10^{-4}\,\mathrm{s}^{-2})$, reduce mixed layer depth and decrease diapycnal diffusivity (Jhugroo et al., 2020). Moreover, the interaction of surface momentum fluxes and horizontal gradients can affect advection patterns in Greater Te-Moana-o-Raukawa/Cook Strait (Jhugroo et al., 2020) and wind-driven turbulence through wind straining in broadly similar systems (Verspecht et al., 2009).

Understanding the balance of processes when boundary-driven turbulence interact in the interior and mixed layers eventually overlap is an important, new component of coastal ocean productivity. During mixed layer overlapping, the mixed water

column suggests fully-homogeneous phytoplankton distributions (Becherer et al., 2022). For periods when surface and bottom mixed layers remain isolated, enhanced turbulence can still modify diapycnal diffusivity at the boundary edges of a weakly to moderately stratified interior layer. Antecedent conditions determine whether the interior layer is maintained or eroded during intensified turbulence episodes, which has implications for biological production in the interior and below the surface mixed layer.

5   Conclusions

Here we present a sizable dataset of $\mathcal{O}(43,000)$ measurements of elevated turbulence from an ocean glider, using a new electromagnetic sensor technology to refine glider speed measurements. This work showcases the value of autonomous sampling platforms for capturing intermittent mixing processes and characterising the vertical structure of mixing in shelf seas. Boundary-driven turbulence interacted in the interior and mixed layers overlapped, under moderate-strong wind and tides forcing, during 35% of a 4 day period in a $\mathcal{O}(200\,\mathrm{m})$ deep system. These observations are novel and inform that the set of ocean conditions that allow for overlapping is more frequent than previously observed and can occur in deeper shelf seas. As revealed by continuous sampling, the interplay of boundary-driven turbulence regulates diffusivity in the coastal ocean interior, potentially influencing primary productivity and air-sea fluxes. Limits for both numerical and field-based stratified turbulence studies were discussed, and optimistically will encourage further exploration of energetic turbulence in coastal seas.

Code and data availability.   The code is available upon request to the corresponding author. Wind and flow speeds (Valcarcel et al., 2022) and ocean microstructure glider (O'Callaghan and Elliott, 2022) datasets are openly available. GOTM versions, test cases, and documentation are available at https://gotm.net.

Appendix A: Additional information on the process of boundary layer overlapping

A1   Interior turbulence interactions and mixing layers

Figure A1 shows the same panels as Figure4c-d, i.e., buoyancy frequency squared N^2 (Fig. A1a) and dissipation rates ϵ (Fig. A1b). Figure A1a is identical to Fig. 4c, with surface (SML) and bottom (BML) mixed layer depths highlighted. As described in Section 2.2 of the main text, the depths of the mixed layers are calculated using a threshold $\Delta\theta = 0.05\,^\circ C$. Figure A1b however highlights surface and bottom mixing layer depths. The depths of the mixing layer are calculated using the standard approach of smoothing the ϵ profiles and using the $\epsilon_p = 3\times10^{-9}\,\mathrm{W\,kg^{-1}}$ threshold (Sutherland et al., 2014; Esters et al., 2018; Giunta and Ward, 2022), also used to detect the duration of the events of interior interaction of turbulence (i-x). The figure illustrates the physical significance of the interior turbulence interaction events, representing mixing layer overlapping, occasionally escalating to mixed layer overlapping (events iii, vi-vii).
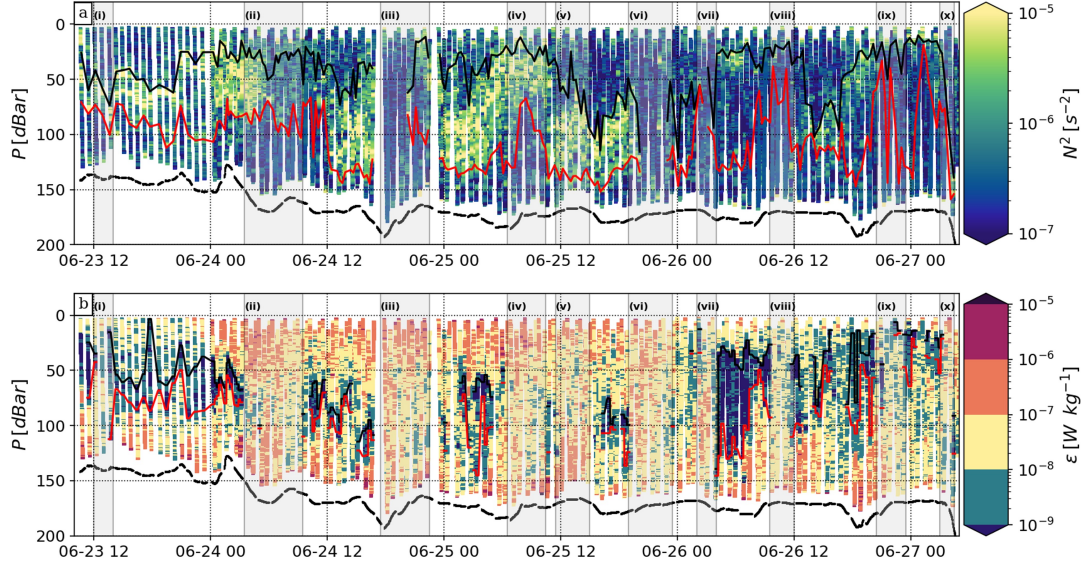
Figure A1. Depth-time series of (a) buoyancy frequency squared N^2 with surface (SML, black line) and bottom (BML, red line) mixed layer depths, respectively; (b) dissipation rates ϵ, with surface (black line) and bottom (red line) mixing layer depths, respectively. Mixed layer depths are computed using a temperature threshold. Mixing layer depths are computed using a dissipation rates, see details in text. Episodes of interior turbulence interactions are shaded and numbered (i-x).

A2   Buoyancy fluxes and restratification

Figure A2 shows buoyancy flux ($b = K_z N^2$) estimates from Ocean Microstructure Glider (OMG) measurements, using two different formulations for diapycnal diffusivity ($K_z = \Gamma \epsilon / N^2$, Osborn (1980)). Figure A2a shows b^{BB}, the buoyancy flux using the Bouffard and Boegman (2013) formulation for K_z and Γ. Figure A2b shows b^O, the buoyancy flux using canonical
545   $\Gamma = 0.2$, parameterization Osborn (1980). Canonical b^O is only shown for comparison, as its variability is by construction equal to that of ϵ, i.e. $b^O = K_z(\Gamma = 0.2) \times N^2 = 0.2 \times \epsilon$. Figure A1a supports the observation of a negligible contribution of buoyancy fluxes to restratification processes. Buoyancy fluxes potentially play a role, however, in providing strengthened stratification to oppose overlapping, e.g. just before event ii, where the conditions for mixed layer overlapping are gathered, but the interior stratification holds (Fig. A2a). Figure A2a further provides context to depth-integrated and depth-averaged results
550   presented in Fig. 9.
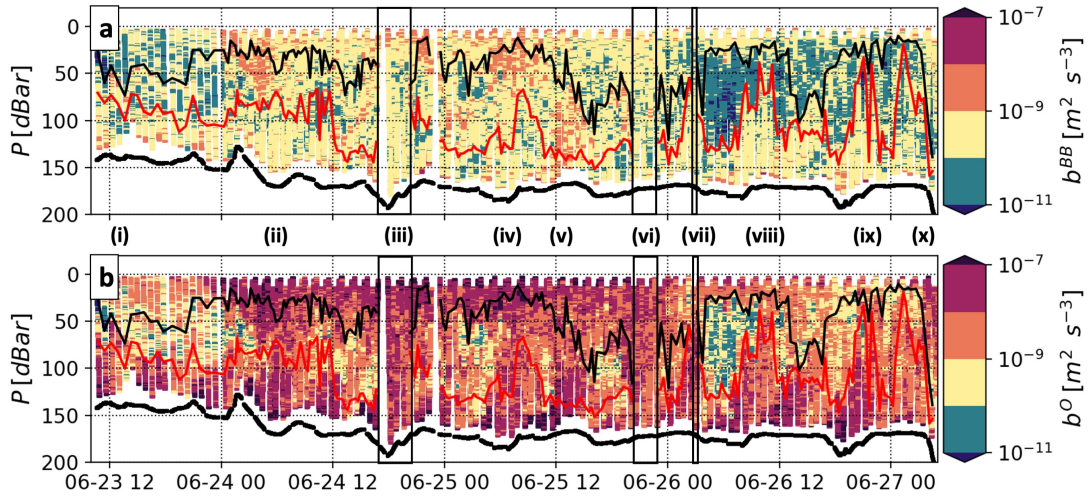
Figure A2. Depth-time series of buoyancy flux $b = K_z N^2$, using the Osborn (1980) formula for $K_z = \Gamma \epsilon / N^2$. (a) $\Gamma = f(Re_b)$ using the Bouffard and Boegman (2013) formula, labelled b^{BB} ; (b) $\Gamma = 0.2$ labelled b^O. In both panels, the thick black dashed line is the seabed, and the surface (SML) and bottom mixed layer (BML) depths are shown with the black and red lines, respectively. Episodes of interior turbulence interactions are numbered (i-x) and the instances when mixed layers overlap episodes are marked with black dashed rectangles.

A3 Turbulence budget

Figure A3 shows the turbulent kinetic energy (tke, k) balance terms computed using the General Ocean Turbulence Model (GOTM). The figure is provided to support a number of observations made in Section 4.3. Specifically, the influence of turbulent transport T_k on the process of interior turbulence interactions and eventual mixed layer overlapping is supported. Six events
555 out of ten events (ii-iii, vi-ix) show enhanced T_k transporting boundary-generated turbulence, eroding interior stratification and connecting in the interior. Events iii and vi-vii notably reflect this pattern, supporting its influence on breaking interior stratification and allowing mixed layers to dramatically entrain and overlap.

Author contributions. This study formed part of the PhD thesis research by A. Valcarcel. All data analysis and manuscript preparation were done by A. Valcarcel with the supervision of C. Stevens, J. O'Callaghan, and S. Suanda. Marsden funding was secured by C. Stevens and J.
560 O'Callaghan. Data collection was done by C. Stevens, J. O'Callaghan, and A. Valcarcel. All authors have read and agreed to the published version of the manuscript.

Competing interests. The authors have no competing interests.
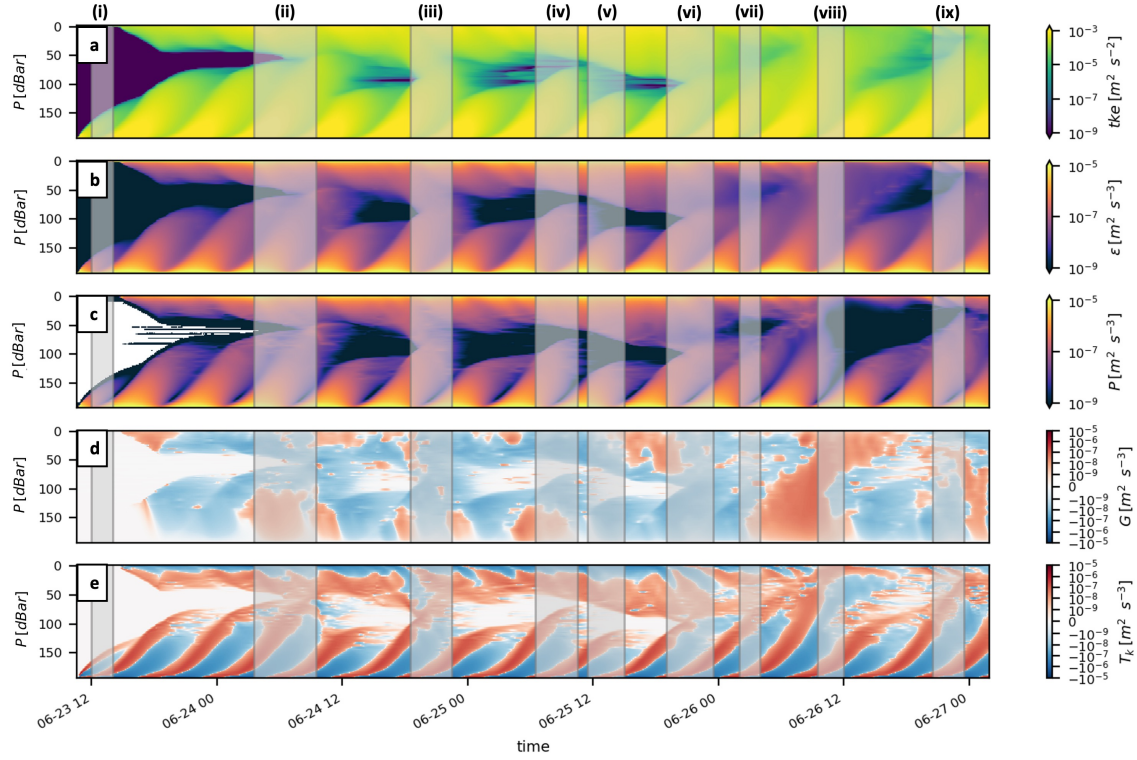
Figure A3. Depth-time series of turbulent kinetic energy (tke) balance terms from the General Ocean Turbulence Model (GOTM). (a) total tke; (b) dissipation rate ϵ; (c) shear production P; (d) buoyancy flux G; (e) total turbulent transport T_k. Episodes of interior turbulence interactions in the OMG observations are highlighted with light grey rectangles and numbered (i-ix, event x is not shown).

Acknowledgements. We acknowledge funding for Project CookieMonster by the Royal Society Te Apārangi Marsden Fund (NIW1702) and the NIWA Capex investment programme. The deployments were conducted by Fiona Elliott and Brett Grant and assistance from the crew of RV Kaharoa. We also acknowledge technical support of Justine McMillan and Evan Cervelli from Rockland Scientific. We also thank the two anonymous reviewers, whose input greatly improved the manuscript.

565

References

Arthur, R. S., Venayagamoorthy, S. K., Koseff, J. R., and Fringer, O. B.: How we compute N matters to estimates of mixing in stratified flows, Journal of Fluid Mechanics, 831, 1–10, https://doi.org/10.1017/jfm.2017.679, 2017.

570   Barry, M. E., Ivey, G. N., Winters, K. B., and Imberger, J.: Measurements of diapycnal diffusivities in stratified fluids, Journal of Fluid Mechanics, https://doi.org/10.1017/S0022112001005080, 2001.

Becherer, J., Burchard, H., Carpenter, J. R., Graewe, U., and Merckelbach, L. M.: The Role of Turbulence in Fueling the Subsurface Chlorophyll Maximum in Tidally Dominated Shelf Seas, Journal of Geophysical Research: Oceans, 127, https://doi.org/10.1029/2022JC018561, 2022.

575   Bianchi, A. A., Bianucci, L., Piola, A. R., Pino, D. R., Schloss, I., Poisson, A., and Balestrini, C. F.: Vertical stratification and air-sea CO_2 fluxes in the Patagonian shelf, Journal of Geophysical Research C: Oceans, 110, 1–10, https://doi.org/10.1029/2004JC002488, 2005.

Bluteau, C. E., Lueck, R. G., Ivey, G. N., Jones, N. L., Book, J. W., and Rice, A. E.: Determining mixing rates from concurrent temperature and velocity measurements, Journal of Atmospheric and Oceanic Technology, 34, 2283–2293, https://doi.org/10.1175/JTECH-D-16-0250.1, 2017.

580   Borges, A. V., Delille, B., and Frankignoulle, M.: Budgeting sinks and sources of CO_2 in the coastal ocean: Diversity of ecosystem counts, Geophysical Research Letters, 32, 1–4, https://doi.org/10.1029/2005GL023053, 2005.

Bouffard, D. and Boegman, L.: A diapycnal diffusivity model for stratified environmental flows, Dynamics of Atmospheres and Oceans, https://doi.org/10.1016/j.dynatmoce.2013.02.002, 2013.

Bowman, M. J., Kibblewhite, A. C., Chiswell, S. M., and Murtagh, R. A.: OCEANOLOGICA ACTA 1983-VOL. 6-N° 2   Shelf fronts and

585   tidal stirring in Greater Cook Strait, Tidal stirring Fronts Stratification Mixing efficiency Cook Strait Marée Fronts Stratification Mélange Détroit de Cook New Zealand ABSTRACT RÉSUMÉ, 1983.

Burchard, H., Bolding, K., and Villarreal, M.: GOTM—A general ocean turbulence model., 1999.

Callaghan, A. H., Ward, B., and Vialard, J.: Influence of surface forcing on near-surface and mixing layer turbulence in the tropical Indian Ocean, Deep-Sea Research Part I: Oceanographic Research Papers, 94, 107–123, https://doi.org/10.1016/j.dsr.2014.08.009, 2014.

590   Canuto, V. M., Howard, A., Cheng, Y., and Dubovikov, M. S.: Ocean turbulence. Part I: One-point closure model-momentum and heat vertical diffusivities, Journal of Physical Oceanography, 31, 1413–1426, https://doi.org/10.1175/1520-0485(2001)031<1413:OTPIOP>2.0.CO;2, 2001.

Caulfield, C.-c. P.: Open questions in turbulent stratified mixing : Do we even know what we do not know ?, Physical Review Fluids, 5, 110 518, https://doi.org/10.1103/PhysRevFluids.5.110518, 2020.

595   Esters, L., Øyvind Breivik, Landwehr, S., Landwehr, S., ten Doeschate, A., Sutherland, G., Christensen, K. H., Bidlot, J., Bidlot, J., Bidlot, J.-R., and Ward, B.: Turbulence Scaling Comparisons in the Ocean Surface Boundary Layer, Journal of Geophysical Research, https://doi.org/10.1002/2017jc013525, 2018.

Fer, I., Peterson, A. K., and Ullgren, J. E.: Microstructure measurements from an underwater glider in the turbulent Faroe Bank Channel overflow, Journal of Atmospheric and Oceanic Technology, 31, 1128–1150, https://doi.org/10.1175/JTECH-D-13-00221.1, 2014.

600   Gargett, A. E. and Wells, J. R.: Langmuir turbulence in shallow water. Part 1. Observations, Journal of Fluid Mechanics, 576, 27–61, https://doi.org/10.1017/S0022112006004575, 2007.

Garrett, C. J., Keeley, J. R., and Greenberg, D. A.: Tidal mixing versus thermal stratification in the bay of fundy and gulf of maine, Atmosphere - Ocean, 16, 403–423, https://doi.org/10.1080/07055900.1978.9649046, 1978.

Gayen, B., Sarkar, S., and Taylor, J. R.: Large eddy simulation of a stratified boundary layer under an oscillatory current, Journal of Fluid Mechanics, 643, 233–266, https://doi.org/10.1017/S002211200999200X, 2010.

Giunta, V. and Ward, B.: Ocean Mixed Layer Depth from Dissipation, Journal Of Geophysical Research: Oceans, https://doi.org/10.1029/2021jc017904, 2022.

Gregg, M., D'Asaro, E., Riley, J., and Kunze, E.: Mixing Efficiency in the Ocean, Annual Review of Marine Science, 10, 443–473, https://doi.org/10.1146/annurev-marine-121916-063643, pMID: 28934598, 2018.

Haas, S., Krien, U., Schachler, B., Bot, S., kyri petrou, Zeli, V., Shivam, K., and Bosch, S.: wind-python/windpowerlib: Silent Improvements (v0.2.1), https://doi.org/10.5281/zenodo.4591809, 2021.

Heath, R. A.: In which direction is the mean flow through Cook Strait, New Zealand — evidence of 1 to 4 week variability?, New Zealand Journal of Marine and Freshwater Research, 20, 119–137, https://doi.org/10.1080/00288330.1986.9516136, 1986.

Hellmann, G.: Über die Bewegung der Luft in den untersten Schichten der Atmosphäre, Kgl, 1919.

Holleman, R. C., Geyer, W. R., and Ralston, D. K.: Stratified Turbulence and Mixing Efficiency in a Salt Wedge Estuary, Journal of Physical Oceanography, 46, 1769–1783, https://doi.org/10.1175/jpo-d-15-0193.1, 2016.

Inall, M. E., Toberman, M., Polton, J. A., Palmer, M. R., Mattias Green, J., and Rippeth, T. P.: Shelf seas baroclinic energy loss: pycnocline mixing and bottom boundary layer dissipation, Journal of Geophysical Research: Oceans, https://doi.org/10.1029/2020jc016528, 2021.

Ioc, Scor, and Iapso: The international thermodynamic equation of seawater – 2010: Calculation and use of thermodynamic properties, Intergovernmental Oceanographic Commission, Manuals and Guides No. 56, p. 196, 2010.

Jabbari, A. and Boegman, L.: Parameterization of oscillating boundary layers in lakes and coastal oceans, Ocean Modelling, 160, 101 780, https://doi.org/https://doi.org/10.1016/j.ocemod.2021.101780, 2021.

Jhugroo, K., O'Callaghan, J., Stevens, C. L., Macdonald, H. S., Elliott, F., and Hadfield, M. G.: Spatial Structure of Low Salinity Submesoscale Features and Their Interactions With a Coastal Current, Frontiers in Marine Science, 7, https://doi.org/10.3389/fmars.2020.557360, 2020.

Jiménez, J.: How linear is wall-bounded turbulence?, Physics of Fluids, 25, https://doi.org/10.1063/1.4819081, 2013.

Jones, C., Creed, E. L., Glenn, S., Kerfoot, J., Kohut, J., Mudgal, C., and Schofield, O.: Slocum Gliders - A Component of Operational Oceanography, Autonomous Undersea Systems Institute Symposium Proceedings, 2005.

JPL MUR MEaSUREs Project: GHRSST Level 4 MUR Global Foundation Sea Surface Temperature Analysis. Ver. 4.1., https://doi.org/10.5067/GHGMR-4FJ04, 2015.

Landahl, M. T.: Linear and non-linear mechanisms in boundary layer turbulence, International journal for numerical methods in fluids, 8, 1183–1184, 1988.

Landahl, M. T.: Boundary layer turbulence regarded as a driven linear system, Physica D, 37, 11–19, 1989.

Li, R., Voulgaris, G., and Wang, Y. P.: Turbulence Structure and Burst Events Observed in a Tidally Induced Bottom Boundary Layer, Journal of Geophysical Research: Oceans, 127, https://doi.org/https://doi.org/10.1029/2021JC018036, e2021JC018036 2021JC018036, 2022.

Lueck: RSI Technical Note 028: Calculating the rate of dissipation of turbulent kinetic energy, p. 18, 2016.

MacKinnon, J. A. and Gregg, M. C.: Spring mixing: Turbulence and internal waves during restratification on the New England shelf, Journal of Physical Oceanography, 35, 2425–2443, https://doi.org/10.1175/JPO2821.1, 2005.

Marsh, R., Hickman, A. E., and Sharples, J.: S2P3-R (v1.0): A framework for efficient regional modelling of physical and biological structures and processes in shelf seas, Geoscientific Model Development, 8, 3163–3178, https://doi.org/10.5194/gmd-8-3163-2015, 2015.

Mashayek, A., Baker, L. E., Cael, B. B., and Caulfield, C. P.: A Marginal Stability Paradigm for Shear-Induced Diapycnal Turbulent Mixing in the Ocean, Geophysical Research Letters, 49, 1–11, https://doi.org/10.1029/2021GL095715, 2022.

Mater, B. D., Venayagamoorthy, S. K., Laurent, L. S., and Moum, J. N.: Biases in thorpe-scale estimates of turbulence dissipation. Part I: Assessments from large-scale overturns in oceanographic data, Journal of Physical Oceanography, 45, 2497–2521, https://doi.org/10.1175/JPO-D-14-0128.1, 2015.

Merckelbach, L., Smeed, D., and Griffiths, G.: Vertical water velocities from underwater gliders, Journal of Atmospheric and Oceanic Technology, 27, 547–563, https://doi.org/10.1175/2009JTECHO710.1, 2010.

Merckelbach, L., Berger, A., Krahmann, G., Dengler, M., and Carpenter, J. R.: A dynamic flight model for Slocum gliders and implications for turbulence microstructure measurements, Journal of Atmospheric and Oceanic Technology, 36, 281–296, https://doi.org/10.1175/JTECH-D-18-0168.1, 2019.

Milne, I. A., Sharma, R. N., and Flay, R. G.: The structure of turbulence in a rapid tidal flow, Proceedings of the Royal Society A: Mathematical, Physical and Engineering Sciences, 473, https://doi.org/10.1098/rspa.2017.0295, 2017.

Monismith, S. G., Koseff, J. R., and White, B. L.: Mixing Efficiency in the Presence of Stratification: When Is It Constant?, Geophysical Research Letters, 45, 5627–5634, https://doi.org/10.1029/2018GL077229, 2018.

Nimmo Smith, W. A. M., Thorpe, S. A., and Graham, A.: Surface effects of bottom-generated turbulence in a shallow tidal sea, Nature, 400, 251–254, https://doi.org/10.1038/22295, 1999.

Oakey, N. S.: Determination of the Rate of Dissipation of Turbulent Energy from Simultaneous Temperature and Velocity Shear Microstructure Measurements, Journal of Physical Oceanography, 1982.

O'Callaghan, J. and Elliott, F.: Ocean Microstructure Glider observations in Cook Strait, New Zealand, [Dataset] SEANOE, https://doi.org/10.17882/89143, 2022.

Orton, P. M., Zappa, C. J., and McGillis, W. R.: Tidal and atmospheric influences on near-surface turbulence in an estuary, Journal of Geophysical Research: Oceans, 115, https://doi.org/10.1029/2010JC006312, 2010.

Osborn, T.: Estimates of the Local Rate of Vertical Diffusion from Dissipation Measurements, 1980.

Peterson, A. K. and Fer, I.: Dissipation measurements using temperature microstructure from an underwater glider, Methods in Oceanography, https://doi.org/10.1016/j.mio.2014.05.002, 2014.

Polzin, K. L. and McDougall, T. J.: Chapter 7 - Mixing at the ocean's bottom boundary, in: Ocean Mixing, edited by Meredith, M. and Naveira Garabato, A., pp. 145–180, Elsevier, ISBN 978-0-12-821512-8, 2022.

Ralston, D. K., Geyer, W. R., Lerczak, J. A., and Scully, M.: Turbulent mixing in a strongly forced salt wedge estuary, Journal of Geophysical Research: Oceans, 115, https://doi.org/10.1029/2009JC006061, 2010.

Rippeth, T. P., Fisher, N. R., and Simpson, J. H.: The cycle of turbulent dissipation in the presence of tidal straining, Journal of Physical Oceanography, 31, 2458–2471, https://doi.org/10.1175/1520-0485(2001)031<2458:tcotdi>2.0.co;2, 2001.

Rockland Scientific: MicroPod-EM: Electromagnetic flow sensor., Rockland Scientific Rep., p. 2, https://rocklandscientific.com/wp-content/uploads/2017/05/RSI-Data-Sheet-MicroPodEM-A4-1_00-web.pdf, 2017.

Rudnick, D. L.: Ocean Research Enabled by Underwater Gliders, Annual Review of Marine Science, 8, 519–541, https://doi.org/https://doi.org/10.1146/annurev-marine-122414-033913, 2016.

Scheifele, B., Waterman, S., Merckelbach, L., and Carpenter, J.: Measuring the Dissipation Rate of Turbulent Kinetic Energy in Strongly Stratified, Low-Energy Environments: A Case Study From the Arctic Ocean, Journal of Geophysical Research: Oceans, https://doi.org/10.1029/2017JC013731, 2018.

Schultze, Merckelbach, L. M., and Carpenter, J. R.: Turbulence and Mixing in a Shallow Shelf Sea From Underwater Gliders, Journal of
680   Geophysical Research: Oceans, 122, 9092–9109, https://doi.org/10.1002/2017JC012872, 2017.

Schultze, Merckelbach, L. M., and Carpenter, J. R.: Storm-induced turbulence alters shelf sea vertical fluxes, Limnology and Oceanography
    Letters, 5, 264–270, https://doi.org/10.1002/lol2.10139, 2020.

Scully, M. E., Geyer, W. R., and Trowbridge, J. H.: The influence of stratification and nonlocal turbulent production on estu-
    arine turbulence: An assessment of turbulence closure with field observations, Journal of Physical Oceanography, 41, 166–185,
685   https://doi.org/10.1175/2010JPO4470.1, 2011.

Sharples, J., Moore, C. M., and Abraham, E. R.: Internal tide dissipation, mixing, and vertical nitrate flux at the shelf edge of NE New
    Zealand, Journal of Geophysical Research: Oceans, 106, 69–81, https://doi.org/10.1029/2000JC000604, 2001.

Shih, L. H., Koseff, J. R., Ivey, G. N., and Ferziger, J. H.: Parameterization of turbulent fluxes and scales using homogeneous sheared stably
    stratified turbulence simulations, Journal of Fluid Mechanics, https://doi.org/10.1017/S0022112004002587, 2005.

690 Simpson, J. H. and Hunter, J. R.: Fronts in the Irish Sea, Nature, 250, 404–406, https://doi.org/10.1038/250404a0, 1974.

Simpson, J. H. and Sharples, J.: Introduction to the Physical and Biological Oceanography of Shelf Seas, Cambridge University Press,
    https://doi.org/10.1017/CBO9781139034098, 2012.

Simpson, J. H., Burchard, H., Fisher, N. R., and Rippeth, T. P.: The semi-diurnal cycle of dissipation in a ROFI: model-measurement
    comparisons, Continental Shelf Research, 22, 1615–1628, https://doi.org/https://doi.org/10.1016/S0278-4343(02)00025-0, proceedings
695   from the Tenth Biennial Conference on the Physics of Estuaries and Coastal Seas, 2002.

Stevens: Residual Flows in Cook Strait, a Large Tidally Dominated Strait, Journal of Physical Oceanography, https://doi.org/10.1175/jpo-d-
    13-041.1, 2014.

Stevens: Turbulent length scales in a fast-flowing, weakly stratified, strait: Cook Strait, New Zealand, Ocean Science, 14, 801–812,
    https://doi.org/10.5194/os-14-801-2018, 2018.

700 Stevens, Smith, M. J., Grant, B., Stewart, C. L., and Divett, T.: Tidal energy resource complexity in a large strait: The Karori Rip, Cook
    Strait, Continental Shelf Research, 33, 100–109, https://doi.org/10.1016/j.csr.2011.11.012, 2012.

Sutherland, G., Christensen, K. H., and Ward, B.: Evaluating Langmuir turbulence parameterizations in the ocean surface boundary layer,
    Journal of Geophysical Research, https://doi.org/10.1002/2013jc009537, 2014.

Thomas, H., Bozec, Y., Elkalay, K., and De Baar, H. J.: Enhanced Open Ocean Storage of CO_2 from Shelf Sea Pumping, Science, 304,
705   1005–1008, https://doi.org/10.1126/science.1095491, 2004.

Thorpe, S. and Deacon, G.: Turbulence and mixing in a Scottish Loch, Philosophical Transactions of the Royal Society of London. Series A,
    Mathematical and Physical Sciences, 286, 125–181, https://doi.org/10.1098/rsta.1977.0112, 1977.

Thorpe, S., Green, J., Simpson, J., Osborn, T., and Nimmo Smith, W.: Boils and turbulence in a weakly stratified shallow tidal sea, Journal
    of Physical Oceanography, 38, 1711–1730, https://doi.org/10.1175/2008JPO3931.1, 2008.

710 Timko, P. G., Arbic, B. K., Hyder, P., Richman, J. G., Zamudio, L., O'Dea, E., Wallcraft, A. J., and Shriver, J. F.: Assessment of shelf sea
    tides and tidal mixing fronts in a global ocean model, Ocean Modelling, 136, 66–84, https://doi.org/10.1016/j.ocemod.2019.02.008, 2019.

Trowbridge, J. H. and Lentz, S. J.: The Bottom Boundary Layer, Annual Review of Marine Science, 10, 397–420,
    https://doi.org/10.1146/annurev-marine-121916-063351, pMID: 29298139, 2018.

Turner, R., Pirooz, A. A., Flay, R. G., Moore, S., and Revell, M.: Use of high-resolution numerical models and statistical approaches to
715   understand New Zealand historical wind speed and gust climatologies, Journal of Applied Meteorology and Climatology, 58, 1195–1218,
    https://doi.org/10.1175/JAMC-D-18-0347.1, 2019.

Umlauf, L. and Burchard, H.: Second-order turbulence closure models for geophysical boundary layers. A review of recent work, Continental Shelf Research, https://doi.org/10.1016/j.csr.2004.08.004, 2005.

Umlauf, L., Burchard, H., and Bolding, K.: GOTM-Sourcecode and Test Case Documentation, Software Manual, p. 346, 2012.

720 Valcarcel, A., Stevens, C., O'Callaghan, J., Suanda, S., and Grant, B.: Wind and current speeds in Cook Strait, New Zealand, [Dataset] SEANOE, https://doi.org/10.17882/89142, 2022.

Vennell, R.: Observations of the phase of tidal currents along a strait, Journal of Physical Oceanography, 28, 1570–1577, https://doi.org/10.1175/1520-0485(1998)028<1570:OOTPOT>2.0.CO;2, 1998a.

Vennell, R.: Oscillating barotropic currents along short channels, Journal of Physical Oceanography, 28, 1561–1569,
725 https://doi.org/10.1175/1520-0485(1998)028<1561:OBCASC>2.0.CO;2, 1998b.

Vennell, R. and Collins, N.: Acoustic Doppler Current Profiler Measurements of Tides in Cook Strait, New Zealand, 1991.

Verspecht, F., Rippeth, T. P., Howarth, M. J., Souza, A. J., Simpson, J. H., and Burchard, H.: Processes impacting on stratification in a region of freshwater influence: Application to Liverpool Bay, Journal of Geophysical Research: Oceans, 114, 1–12, https://doi.org/10.1029/2009JC005475, 2009.

730 Wang, J., Greenan, B. J., Lu, Y., Oakey, N. S., and Shaw, W. J.: Layered mixing on the New England Shelf in summer, Journal of Geophysical Research: Oceans, 119, 5776–5796, https://doi.org/10.1002/2014JC009947, 2014.

Watanabe, M. and Hibiya, T.: Global estimates of the wind-induced energy flux to inertial motions in the surface mixed layer, Geophysical Research Letters, 29, 2–5, https://doi.org/10.1029/2001GL014422, 2002.

Waterhouse, A. F., Mackinnon, J. A., Nash, J. D., Alford, M. H., Kunze, E., Simmons, H. L., Polzin, K. L., Laurent, L. C., Sun, O. M., Pinkel,
735 R., Talley, L. D., Whalen, C. B., Huussen, T. N., Carter, G. S., Fer, I., Waterman, S., Naveira Garabato, A. C., Sanford, T. B., and Lee, C. M.: Global patterns of diapycnal mixing from measurements of the turbulent dissipation rate, Journal of Physical Oceanography, 44, 1854–1872, https://doi.org/10.1175/JPO-D-13-0104.1, 2014.

Wesson, J. C. and Gregg, M. C.: Mixing at Camarinal Sill in the Strait of Gibraltar, Journal of Geophysical Research, 99, 9847–9878, https://doi.org/10.1029/94JC00256, 1994.

740 Williams, C., Sharples, J., Mahaffey, C., and Rippeth, T.: Wind-driven nutrient pulses to the subsurface chlorophyll maximum in seasonally stratified shelf seas, Geophysical Research Letters, 40, 5467–5472, https://doi.org/10.1002/2013GL058171, 2013.

Wu, K.-T., Tsai, C. W., and Wu, M.-J.: Probabilistic Characterization of Sweep and Ejection Events in Turbulent Flows and Its Implications on Sediment Transport, Water Resources Research, 58, https://doi.org/10.1029/2021WR030417, 2022.

Yan, C., McWilliams, J. C., and Chamecki, M.: Overlapping Boundary Layers in Coastal Oceans, Journal of Physical Oceanography, 52,
745 627–646, https://doi.org/10.1175/JPO-D-21-0067.1, 2022.

Zeldis, J. R., Hadfield, M. G., and Booker, D. J.: Influence of climate on pelorus sound mussel aquaculture yields: Predictive models and underlying mechanisms, Aquaculture Environment Interactions, 4, 1–15, https://doi.org/10.3354/aei00066, 2013.

Zhang, Y. and Tian, J.: Enhanced turbulent mixing induced by strong wind on the South China Sea shelf, Ocean Dynamics, 64, 781–796, https://doi.org/10.1007/s10236-014-0710-0, 2014.